

Lukas Wielandner, BSc

# **Implementation and Validation of Reaction Kinetics for Methane Steam Reforming in CFD Simulation**

## **Master's Thesis**

to achieve the university degree of

Diplom-Ingenieur

Master's degree programme: Technical Physics

submitted to

**Graz University of Technology**

Supervisor

Univ.-Prof. Dipl.-Phys. Dr.rer.nat. Wolfgang von der Linden

Institute of Theoretical and Computational Physics

Co-Supervisor

DI Michael Seidl

AVL

Graz, September 2018



## **AFFIDAVIT**

I declare that I have authored this thesis independently, that I have not used other than the declared sources/resources, and that I have explicitly indicated all material which has been quoted either literally or by content from the sources used. The text document uploaded to TUGRAZonline is identical to the present master's thesis dissertation.

---

Date

---

Signature





---

# Abstract

---

Methane steam reforming (MSR) is a key process for the generation of hydrogen, which is required for various applications. This thesis addresses the reforming process of a solid oxide fuel cell (SOFC) system. The aim of this thesis is to implement and validate the reaction kinetics for MSR in the AVL CFD simulation software FIRE. So far, FIRE has mostly been used for the simulation of combustion processes but due to the growing influence of fuel cells, new models should be included to explain reforming processes. Within this thesis, methane steam reforming is described with three partial reactions, which depict the formation of hydrogen and the water gas shift. Firstly, a literature benchmark was done to validate the model. Afterwards it was used to simulate a reforming reactor, whose geometric and catalytic parameters as well as the operating temperature differ from the literature benchmark, but were backed by experimental data. The influence of the variation of the catalytic parameters was investigated and a model could be derived that fits both the literature benchmark as well as the measurements done by AVL.



---

# Contents

---

<b>1</b>	<b>Introduction</b>	<b>1</b>
<b>2</b>	<b>Theory</b>	<b>3</b>
2.1	Solid Oxide Fuel Cell . . . . .	3
2.2	CFD Solver . . . . .	4
2.2.1	Underrelaxation Factors . . . . .	5
2.2.2	Lagrangian and Eulerian Frame of Reference. . . . .	5
2.3	Stress Tensor $\sigma_{ij}$ . . . . .	6
2.3.1	Analysis of Fluid Motion . . . . .	7
2.3.2	Relation between Stress and Rate of Strain . . . . .	9
2.4	Laws of Conservation. . . . .	11
2.4.1	Conservation of Mass . . . . .	11
2.4.2	Momentum Equation . . . . .	12
2.4.3	Energy Equation. . . . .	13
2.5	Navier-Stokes Equation . . . . .	15
2.5.1	Statistical description . . . . .	16
2.6	Species Transport Module. . . . .	17
2.7	Aftertreatment Module . . . . .	18
2.7.1	Solid energy balance equation. . . . .	19
2.7.2	Chemical Reaction Rate Calculation . . . . .	20
2.7.3	Transfer Coefficients . . . . .	22
2.8	Calculation of the Equilibrium Constant . . . . .	23

<b>3</b>	<b>Model and Methods</b>	<b>27</b>
3.1	Catalytic Parameters . . . . .	27
3.1.1	Settings and Parameters for the Benchmark Model . . . . .	28
3.1.2	Settings and Parameters for the AVL Reformer. . . . .	29
3.2	Reaction Kinetics and Model Development . . . . .	29
3.2.1	Implementation of the Kinetic Model. . . . .	31
3.3	Mesh and Solver Settings . . . . .	32
3.3.1	Benchmark Model . . . . .	33
3.3.2	AVL reformer model . . . . .	35
3.4	Optimization settings. . . . .	36
<b>4</b>	<b>Results and Discussion</b>	<b>37</b>
4.1	Literature benchmark . . . . .	38
4.2	AVL reformer . . . . .	41
4.2.1	Reaction kinetic parameters of Hoang . . . . .	41
4.2.2	Reaction Kinetic Parameters of Xu . . . . .	43
4.2.3	Optimized activation energies $E_i$ . . . . .	44
4.2.4	Equilibrium constant . . . . .	46
4.2.5	Parameter study with $K_{\text{fit}}$ . . . . .	52
<b>5</b>	<b>Summary and Outlook</b>	<b>57</b>
	<b>Bibliography</b>	<b>61</b>

# CHAPTER 1

---

## Introduction

---

Methane steam reforming (MSR) is a key process for the generation of hydrogen which is required for various applications. This thesis addresses the reforming process of a solid oxide fuel cell (SOFC) system as described in section 2.1.

The aim of this thesis is to implement and validate the reaction kinetics for MSR in the AVL CFD simulation software FIRE. So far, FIRE has mostly been used for the simulation of combustion processes but due to the growing influence of fuel cells, new models should be included to explain reforming processes.

This topic has long been studied in literature. In 1780, the production of combustible gas was observed for the first time by Fontana. In the 19<sup>th</sup> century, the first patents were filed concerning the generation of hydrogen. [1]

The first extensive study concerning the kinetics of the MSR reaction was published by Akers and Champ in 1955 [2]. In this study, Akers and Champ developed a first order model for the conversion of methane. Their results indicated that the rate of reaction was directly proportional to the partial pressure of methane. Afterwards many publications followed with different kinetic models, for example the study of Bodrov in 1964 [1] or Ross and Steel in 1972 [3]. The review from Elnshaie from 1988 [4], gives a good overview how the kinetic models differ.

In 1989, Xu and Froment developed a kinetic model which is still state of the art [5]. Following publications like Hoang [6] or Singh [7] changed only coefficients which depend on the catalytic material but did not modify the equations for the rate of reactions.

MSR is nowadays explained with three partial reactions given in Table 1.1.

**Table 1.1:** Partial reactions for MSR.

No.	Reaction
1	$\text{CH}_4 + \text{H}_2\text{O} \rightleftharpoons \text{CO} + 3\text{H}_2$
2	$\text{CO} + \text{H}_2\text{O} \rightleftharpoons \text{CO}_2 + \text{H}_2$
3	$\text{CH}_4 + 2\text{H}_2\text{O} \rightleftharpoons \text{CO}_2 + 4\text{H}_2$

Reaction one and three are the governing reactions for the production of hydrogen and reaction two describes the water-gas shift.

There are publications about CFD simulation for MSR like the one of Kuroki [8] but those simulations are done after extracting the kinetic parameters with expensive and long lasting experiments or simulating already published articles. Within this thesis, a set of parameters should be found that would reduce significantly tests for a viable catalyst used by AVL. The objective lays on how specific parameters influence the outcome of the simulation. With this knowledge, it should be possible to adjust the model to fit measured data for MSR for any catalytic material with arbitrary geometries. On the other hand, the geometric optimization of a reformer design should be applicable with a valid set of reaction kinetic parameters.

# CHAPTER 2

---

## Theory

---

This chapter gives an overview about a solid oxide fuel cell, the mathematical models used in computational fluid dynamic simulations and explains how they can be derived.

In the first section, the working principle of an SOFC is explained. The second section, section 2.2, gives an introduction about the solver of the computational fluid dynamics (CFD) software FIRE, shows which approaches are made and states the difference between the Lagrangian and Eulerian frame of reference. Additionally, underrelaxation factors are explained. Section 2.3 introduces the stress tensor and shows, how it can be related to the motion of a fluid. The forth section, section 2.4, states the laws of conservation and explicates how they are derived. Those laws are essential for the formulation of the Navier-Stokes equation, which is explained in the section afterwards. The sections 2.6 "Species Transport Module" and 2.7 "Aftertreatment Module" show how species transport phenomena as well as catalytic conversion of species and heat transfer are treated in FIRE. Section 2.8 describes how the equilibrium constant of a chemical reaction can be derived.

### 2.1 Solid Oxide Fuel Cell

SOFCs convert chemical energy directly into electrical energy and are not restricted by the Carnot efficiency like heat engines. In an SOFC, the electrolyte consists of a non porous metal oxide, which is placed between the anode and the cathode. The operating temperature is between 600 °C and 1000 °C, where ionic conduction by oxygen ions takes place [9]. The most common reductant (fuel) and oxidant are hydrogen and ambient air.

For a convenient storage and transportation, hydrocarbons can be used as fuels, but they have to be converted into an SOFC compatible gas mixture for further use. This is done by a catalytic reformer depicted in Figure 2.1.

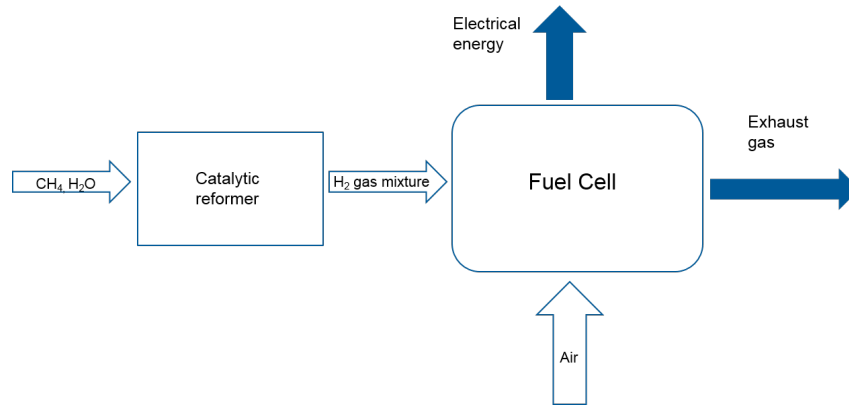


**Figure 2.1:** Gas conversion process of a SOFC system. The methane and water mixture is converted into an SOFC compatible gas mixture in the catalytic reformer. The generated hydrogen and carbon monoxide is used to power the fuel cell.

At the cathode, the reduction of oxygen into oxygen ions takes place. These ions can diffuse through the electrolyte and react with hydrogen. As a result of this reaction, water is generated and two electrons are given off, which flow through an external circuit. The reactant flow in an SOFC can be described as in Figure 2.2.

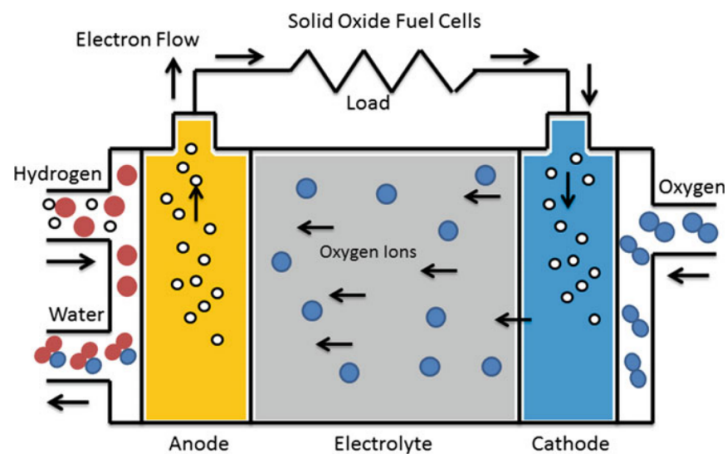


**Figure 2.2:** Reactant flow in an SOFC. The figure is taken from Bagheri [10]

## 2.2 CFD Solver

The AVL CFD Solver is based on the Finite Volume approach. The solver rests on general conservation laws describing the behaviour of matter when it interacts with its surrounding. These laws are adaptable for solids and fluids. The most common formulations of

the conservation laws are done in the Lagrangian frame of reference, which is suitable for the description of properties and dynamics of solids. To describe fluid flow and its transport processes, the Euler frame of reference is preferred. This is realised by the 'Finite Volume approach', which differs from other numerical methods by the fact that the conservation equations are integrated before discretization over the finite control volumes. Those volumes are cells which are generated by the numerical mesh. [11]

### 2.2.1 Underrelaxation Factors

The solution of the  $k^{th}$  iteration depends on the values of the  $(k-1)^{th}$  iteration but this change of variable values is also limited by an underrelaxation factor  $\alpha_\phi$ , which has a value between 0 and 1 to ensure convergence. The values of the  $k^{th}$  iteration  $\phi^k$  are calculated by adding the value of the previous iteration to the difference of  $k^{th}$  iteration minus the previous iteration times a scaling factor which is the underrelaxation factor. For a value smaller than one, this factor reduces oscillations in the solution and increases the stability of the solution. On the other hand, it can decrease the speed of convergence. The value for the  $k^{th}$  iteration is calculated by solving the following equation.

$$\phi^k = \phi^{k-1} + \alpha_\phi (\phi^{new} - \phi^{k-1}) \quad (2.1)$$

### 2.2.2 Lagrangian and Eulerian Frame of Reference

The idea of the Lagrangian way of representation is to follow the path of individual objects and keep track of the position and velocity vector of each object [12].

It is difficult to define and identify moving fluid particles, thus a more convenient way to represent the motion of a fluid is the Euler description.

In this case, a finite volume of the fluid is defined, through which the fluid flows in and out. Instead of keeping track of all the positions and velocities, pressure and velocity fields are defined in the specified volume. The fluid parameters are therefore functions of time and coordinates of a specific point in space. In other words, the fluid parameters at this point are investigated over time.

Even though the Eulerian representation is a more convenient way for simulations, it is still essential to consider the rate of change of quantities following a fluid particle which

leads to the definition of the *material derivative*. This is the rate of change in time following a fluid particle expressed in Euler coordinates.  $F$  is a quantity following a fluid particle that is described in both frames.

$$F = F_L(x_i^0, \hat{t}) = F_E(x_i, t) = F_E(r_i(x_i, \hat{t}), t) \quad (2.2)$$

The rate of change can be written as

$$\frac{\partial F}{\partial \hat{t}} = \frac{\partial F_E}{\partial x_i} \frac{\partial r_i}{\partial \hat{t}} + \frac{\partial F_E}{\partial t} \frac{\partial t}{\partial \hat{t}} = \frac{\partial F_E}{\partial t} + u_i \frac{\partial F_E}{\partial x_i} \quad (2.3)$$

The material derivative  $\frac{D}{Dt}$  is therefore defined as

$$\frac{\partial}{\partial \hat{t}} \equiv \frac{D}{Dt} = \frac{\partial}{\partial t} + u_i \frac{\partial}{\partial x_i} = \frac{\partial}{\partial t} + (\mathbf{u} \nabla) \quad (2.4)$$

### 2.3 Stress Tensor $\sigma_{ij}$

The introduction of stress is a convenient way to describe the transmission of forces through a medium which act on its boundaries. The theory of the stress tensor is summarised by means of Ferziger [13], Hirsch [14] and Pedlosky [15].

The total force on a given fluid element  $\int_V \mathbf{F} dV$  can be transformed into a surface integral by applying the divergence theorem.

$$\oint \sigma_{ij} dA_j = \int \frac{\partial \sigma_{ij}}{\partial x_j} dV = \int F_i dV \quad (2.5)$$

The stress tensor is not generally diagonal but it can be proven that it is always possible to find a transformation matrix  $a_{ij}$  that diagonalises the stress tensor in a new frame.

$$\sigma'_{ij} = a_{ik} a_{jl} \sigma_{kl} = \sigma_{(j) \delta_{ij}} = \begin{pmatrix} \sigma_1 & 0 & 0 \\ 0 & \sigma_2 & 0 \\ 0 & 0 & \sigma_3 \end{pmatrix} \quad (2.6)$$

The value where all diagonal entries are the same is called *static pressure*.

$$\sigma_{ij} = -p \delta_{ij} \quad (2.7)$$

For a fluid at rest,  $p$  is the pressure in the fluid and also the thermodynamic pressure. If a fluid is moving, the pressure does not have to be the thermodynamic pressure, as it is defined as the average normal forces on a fluid element.

The average normal stress is

$$\frac{\sigma_{ii}}{3} = \frac{1}{3}(\sigma_{11} + \sigma_{22} + \sigma_{33}) \quad (2.8)$$

which is equal to  $-p$  only for simple monoatomic gases. In general the thermodynamic pressure deviates from the average normal stress.

It is possible to split the stress tensor into two parts where  $\tau_{ij}$  (deviatoric stress) is defined as the difference between the pressure and the total stress.

$$\sigma_{ij} = -p\delta_{ij} + \tau_{ij} \quad (2.9)$$

Depending on the definition of the pressure the trace of  $\tau_{ij}$  vanishes or not. If the pressure is defined as the average normal stress, the trace of  $\tau_{ij}$  is zero and the pressure does not have to be equal to the thermodynamic pressure.

### 2.3.1 Analysis of Fluid Motion

To achieve the goal of relating the stress tensor to the fluid motion, the motion near a point  $x_i$  is considered. The velocity can be written in terms of a Taylor series. Due to a small region, the series is truncated after the first term

$$u_i(x_j + \delta x_j) \simeq u_i(x_j) + \frac{\partial u_i}{\partial x_j} \delta x_j \quad (2.10)$$

where  $\frac{\partial u_i}{\partial x_j}$  is the deformation tensor, which influences the deviatoric stress tensor.

The velocity can be split up into

$$u_i(x_j + \delta x_j) = u_i(x_j) + \delta u_i(x_j)$$

which leads to

$$\delta u_i(x_j) = \frac{\partial u_i}{\partial x_j} \delta x_j \quad (2.11)$$

The velocity derivation, like any other matrix, can be decomposed in a sum of a symmetric and an antisymmetric matrix.

$$\delta u_i(x_j) = \underbrace{\frac{1}{2} \left[ \frac{\partial u_i}{\partial x_j} + \frac{\partial u_j}{\partial x_i} \right]}_{\text{symmetric}} \delta x_j + \underbrace{\frac{1}{2} \left[ \frac{\partial u_i}{\partial x_j} - \frac{\partial u_j}{\partial x_i} \right]}_{\text{antisymmetric}} \delta x_j \quad (2.12)$$

The symmetric tensor

$$e_{ij} = \frac{1}{2} \left[ \frac{\partial u_i}{\partial x_j} + \frac{\partial u_j}{\partial x_i} \right]$$

is called the *rate of strain tensor* because it can be shown that the diagonal elements represent the rate of stretching of a fluid element along the corresponding axes. The off diagonal elements represent the rate of shear strain of a fluid element [15].

The antisymmetric tensor

$$\xi_{ij} = \frac{1}{2} \left[ \frac{\partial u_i}{\partial x_j} - \frac{\partial u_j}{\partial x_i} \right]$$

can be related to the *vorticity*.

$\xi_{ij}$  has the same components as the vector

$$\frac{1}{2} \vec{\omega} = \frac{1}{2} \nabla \times \vec{u} \quad (2.13)$$

with

$$\omega_i = \varepsilon_{ijk} \frac{\partial u_k}{\partial x_j} \quad (2.14)$$

In general,  $\xi_{ij}$  can be written as

$$\xi_{ij} = -\frac{1}{2} \varepsilon_{ijk} \omega_k \quad (2.15)$$

This derives from

$$\xi_{ij} = -\frac{1}{2} \varepsilon_{ijk} \omega_k = -\frac{1}{2} \varepsilon_{ijk} \varepsilon_{klm} \frac{\partial u_m}{\partial x_l} = -\frac{1}{2} \varepsilon_{kij} \varepsilon_{klm} \frac{\partial u_m}{\partial x_l} \quad (2.16)$$

and leads with

$$\varepsilon_{kij} \varepsilon_{klm} = \begin{vmatrix} \delta_{il} & \delta_{lj} \\ \delta_{im} & \delta_{jm} \end{vmatrix} = \delta_{il} \delta_{jm} - \delta_{im} \delta_{lj} \quad (2.17)$$

to

$$\begin{aligned}\xi_{ij} &= -\frac{1}{2} (\delta_{il}\delta_{jm} - \delta_{im}\delta_{lj}) \frac{\partial u_m}{\partial x_l} \\ \xi_{ij} &= -\frac{1}{2} \left( \delta_{il}\delta_{jm} \frac{\partial u_m}{\partial x_l} - \delta_{im}\delta_{lj} \frac{\partial u_m}{\partial x_l} \right) \\ \xi_{ij} &= -\frac{1}{2} \left[ \frac{\partial u_j}{\partial x_i} - \frac{\partial u_i}{\partial x_j} \right]\end{aligned}\tag{2.18}$$

Equation 2.19 shows that the deviation of the velocity is proportional to the antisymmetric tensor.

$$\delta u^{(\vec{a})} = \xi_{ij} \delta x_j = \frac{1}{2} \vec{\omega} \times \delta \vec{x}\tag{2.19}$$

It can be seen as the displacement velocity due to rotation. It is a pure rotation due to the fact that there is no change of the length of  $\delta \vec{x}$  and only a change of direction.

### 2.3.2 Relation between Stress and Rate of Strain

To relate the fluid velocity to the stress tensor, it has to be assumed that the stress tensor is a function of the deformation tensor and that the fluid is isotropic with regard to the relation between stress and rate of strain. The relation between stress and rate of strain is expected to be homogeneous and linear. This yields a general relation between the deviatoric stress and the deformation tensor.

$$\tau_{ij} = T_{ijkl} \frac{\partial u_k}{\partial x_l}\tag{2.20}$$

$T_{ijkl}$  is an isotropic fourth order tensor. The most general isotropic second order tensor is  $\delta_{ij}$ . To find its fourth order equivalent, the scalar constructed by the inner product of  $T_{ijkl}$  with the vectors  $A_i$ ,  $B_i$ ,  $C_i$  and  $D_i$  is considered.

$$S = T_{ijkl} A_i B_j C_k D_l\tag{2.21}$$

Because  $T_{ijkl}$  is isotropic,  $S$  should only depend on the orientation of the vectors to one another.

$$S = \alpha(\vec{A} \cdot \vec{B})(\vec{C} \cdot \vec{D}) + \beta(\vec{A} \cdot \vec{C})(\vec{B} \cdot \vec{D}) + \gamma(\vec{A} \cdot \vec{D})(\vec{C} \cdot \vec{B})\tag{2.22}$$

$$T_{ijkl}A_iB_jC_kD_l = \alpha A_iB_iC_jD_j + \beta A_iB_iC_jD_j + \gamma A_iB_iC_jD_j$$

$$T_{ijkl}A_iB_jC_kD_l = A_iB_jC_kD_l [\alpha\delta_{ij}\delta_{kl} + \beta\delta_{ik}\delta_{lj} + \gamma\delta_{il}\delta_{jk}]$$

$$T_{ijkl} = \alpha\delta_{ij}\delta_{kl} + \beta\delta_{ik}\delta_{lj} + \gamma\delta_{il}\delta_{jk} \quad (2.23)$$

This tensor can be simplified by applying the constraint of symmetry  $T_{ijkl} = T_{jikl}$

$$\cancel{\alpha\delta_{ij}\delta_{kl}} + \beta\delta_{ik}\delta_{lj} + \gamma\delta_{il}\delta_{jk} = \cancel{\alpha\delta_{ji}\delta_{kl}} + \beta\delta_{jk}\delta_{li} + \gamma\delta_{jl}\delta_{ik}$$

$$\beta\delta_{ik}\delta_{lj} + \gamma\delta_{il}\delta_{jk} = \beta\delta_{jk}\delta_{li} + \gamma\delta_{jl}\delta_{ik}$$

$$(\beta - \gamma)\delta_{ik}\delta_{lj} = (\beta - \gamma)\delta_{jk}\delta_{il} \quad (2.24)$$

This is only true if  $\beta = \gamma$ .

$$T_{ijkl} = \alpha\delta_{ij}\delta_{kl} + \beta(\delta_{ik}\delta_{lj} + \delta_{jk}\delta_{il}) \quad (2.25)$$

With  $\sigma_{ij} = -p\delta_{ij} + \tau_{ij}$  and  $\tau_{ij} = T_{ijkl}\frac{\partial u_k}{\partial x_l}$

$$\sigma_{ij} = -p\delta_{ij} + [\alpha\delta_{ij}\delta_{kl} + \beta(\delta_{ik}\delta_{lj} + \delta_{jk}\delta_{il})] \frac{\partial u_k}{\partial x_l}$$

$$\sigma_{ij} = -p\delta_{ij} + \alpha\delta_{ij}\frac{\partial u_k}{\partial x_k} + \beta\left(\frac{\partial u_i}{\partial x_j} + \frac{\partial u_j}{\partial x_i}\right)$$

$$\sigma_{ij} = -p\delta_{ij} + 2\mu e_{ij} + \lambda e_{kk}\delta_{ij} \quad (2.26)$$

Due to the fact that the pressure is invariant of the coordinate system since the trace of  $\sigma_{ij}$  is an invariant scalar, the trace of the deviatoric stress must be zero

$$\tau_{ii} = 2\mu e_{ij} + \lambda e_{kk}\delta_{ij} = e_{jj}[2\mu + 3\lambda] = 0 \quad (2.27)$$

which results in  $\lambda = -\frac{2}{3}\mu$ , where  $\mu$  is the coefficient of the viscosity.

Equation 2.26 is only valid if the pressure is defined as the thermodynamic pressure. If this is not the case, it has to be considered that the difference between the thermodynamic pressure  $p_e$  and the mechanically defined pressure is depending on the deformation tensor.

$$p = p_e - \eta \frac{\partial u_i}{\partial x_j} \delta_{ij} = p_e - \eta \frac{\partial u_j}{\partial x_j} \quad (2.28)$$

As a result the stress tensor becomes

$$\sigma_{ij} = -p_e \delta_{ij} + 2\mu e_{ij} + \left( \eta - \frac{2}{3}\mu \right) e_{kk} \delta_{ij} \quad (2.29)$$

For a monoatomic gas  $\eta = 0$ .

Those derived equations for the stress tensor are needed for the formulation and understanding of the conservation laws in the following sections.

## 2.4 Laws of Conservation

Fundamental physical laws of conservation state, that the rate of change of an extensive property like energy or mass is a consequence of the interaction between a system and its surroundings. This section is written with the help of following literature: Henningson [12], Ferziger [13], Hirsch [14] and Kochukhov [16].

The following three subsections explain the main conservation laws, namely the conservation of mass, the conservation of momentum and the conservation of energy.

### 2.4.1 Conservation of Mass

The conservation of mass states that the mass of a fluid containing the same particles at all time in a specific volume is constant. The mass of the fluid is defined as  $\int_V \rho dV$ .

$$\frac{D}{Dt} \int_V \rho dV = \int_V \frac{\partial \rho}{\partial t} + \frac{\partial}{\partial x_k} (u_k \rho) dV = 0 \quad (2.30)$$

The integrand has to be zero because the equation has to be valid for an arbitrary volume.

$$\frac{\partial \rho}{\partial t} + \frac{\partial}{\partial x_k} (u_k \rho) = 0 = \frac{\partial \rho}{\partial t} + \rho \frac{\partial u_k}{\partial x_k} + u_k \frac{\partial \rho}{\partial x_k} = \frac{D\rho}{Dt} + \rho \frac{\partial u_k}{\partial x_k} \quad (2.31)$$

which leads to

$$\frac{D\rho}{Dt} = -\rho \frac{\partial u_k}{\partial x_k} \quad (2.32)$$

### 2.4.2 Momentum Equation

The momentum equation describes the time rate of change of momentum in a material region. It is equal to the sum of the forces.

$$\frac{D}{Dt} \int_V \rho u_i dV = \int_V \rho F_i dV + \int_S R_i dS \quad (2.33)$$

$F_i$  ... body force per unit mass  
 $R_i$  ... surface force per unit area  
 $\rho u_i$  ... momentum per unit volume

With the help of the Reynold's theorem, it is possible to place the material derivative inside the integral.

$$\int_V \rho \frac{Du_i}{Dt} dV = \int_V \rho F_i dV + \int_S R_i dS \quad (2.34)$$

The total surface force  $R_i$  can be written in terms of the components of the stress tensor.

$$R_i = \sigma_{i1}n_1 + \sigma_{i2}n_2 + \sigma_{i3}n_3 \quad (2.35)$$

A rewriting of the above equation yields

$$\int_V \rho \frac{Du_i}{Dt} dV = \int_V \rho F_i dV + \int_S \sigma_{ij}n_j dS = \int_V \left[ \rho F_i + \frac{\partial \sigma_{ij}}{\partial x_j} \right] dV \quad (2.36)$$

The equation has to be valid for an arbitrary volume so the integrand has to be zero.

$$\rho \frac{Du_i}{Dt} = \rho F_i + \frac{\partial}{\partial x_j} (-p\delta_{ij} + \tau_{ij}) = \rho F_i - \frac{\partial p}{\partial x_i} + \frac{\partial \tau_{ij}}{\partial x_j} \quad (2.37)$$

Or in other terms

$$\rho \frac{Du_i}{Dt} = \rho F_i - \frac{\partial p}{\partial x_i} + \frac{\partial}{\partial x_j} \left[ \mu \left( \frac{\partial u_i}{\partial x_j} + \frac{\partial u_j}{\partial x_i} - \frac{2}{3} \frac{\partial u_k}{\partial x_k} \delta_{ij} \right) \right] \quad (2.38)$$

It can also be written as

$$\rho \frac{D\mathbf{u}}{Dt} = \frac{\partial \mathbf{u}}{\partial t} + (\mathbf{u} \nabla) \mathbf{u} = -\frac{\nabla p}{\rho} + \rho \mathbf{F} \quad (2.39)$$

which is the **Euler equation** if external forces and friction is set to zero.

$$\rho \frac{D\mathbf{u}}{Dt} = \frac{\partial \mathbf{u}}{\partial t} + (\mathbf{u} \nabla) \mathbf{u} = 0 \quad (2.40)$$

### 2.4.3 Energy Equation

The rate of change of energy of a particle is equal to the rate that energy is received by heat and work transfer by said particle. With the relation of  $R_i = \sigma_{ij} n_j$ , the following equation can be derived

$$\frac{D}{Dt} \int_V \rho \left[ e + \frac{1}{2} u_i u_i \right] dV = \int_V \rho u_i F_i dV + \int_S [n_i \sigma_{ij} u_j - n_i q_i] dS \quad (2.41)$$

$$\begin{aligned} \rho \left[ e + \frac{1}{2} u_i u_i \right] dV & \dots \text{ energy of particle} \\ \rho u_i F_i dV & \dots \text{ work rate of } F_i \text{ on that particle} \\ u_j R_j dS & \dots \text{ work rate of } R_j \text{ on that particle} \\ n_i q_i dS & \dots \text{ heat loss from surface} \end{aligned}$$

This equation can be reformulated to

$$\frac{D}{Dt} \int_V \rho \left[ e + \frac{1}{2} u_i u_i \right] dV = \int_V \left[ \rho u_i F_i + \frac{\partial}{\partial x_i} (\sigma_{ij} u_j - q_i) \right] dV \quad (2.42)$$

The integrand of the equation has to be zero to be valid for an arbitrary volume.

$$\rho \frac{D}{Dt} \left[ e + \frac{1}{2} u_i u_i \right] = \rho u_i F_i - \frac{\partial}{\partial x_i} (p u_i) + \frac{\partial}{\partial x_i} (\tau_{ij} u_j) - \frac{\partial q_i}{\partial x_i} \quad (2.43)$$

This equation can be split into parts of the kinetic energy  $\frac{1}{2} u_i u_i$  and the thermal energy  $e$

The kinetic (mechanical) part can be developed by a dot-product between equation 2.37 and  $u_i$ .

$$\rho \frac{D}{Dt} \left( \frac{1}{2} u_i u_i \right) = \rho F_i u_i - u_i \frac{\partial p}{\partial x_i} + u_i \frac{\partial \tau_{ij}}{\partial x_j} \quad (2.44)$$

The thermal energy can be derived by subtracting the mechanical energy from the total energy (equation 2.43 - equation 2.44).

$$\rho \frac{De}{Dt} = -p \frac{\partial u_i}{\partial x_i} + \tau_{ij} \frac{\partial u_i}{\partial x_j} - \frac{\partial q_i}{\partial x_i} + \underbrace{\left( u_j \frac{\partial \tau_{ij}}{\partial x_i} - u_i \frac{\partial \tau_{ij}}{\partial x_j} \right)}_{\tau_{ij} = \tau_{ji}} \quad (2.45)$$

In equation 2.43, the two not obvious terms can be split into thermal terms and mechanical terms.

- Thermal terms  
related to forces and deformations
- Mechanical terms  
related to velocities and force gradients

	thermal	mechanical
$-\frac{\partial}{\partial x_i}(\rho u_i)$	$= -\rho \frac{\partial u_i}{\partial x_i}$	$-u_i \frac{\partial \rho}{\partial x_i}$
$\frac{\partial}{\partial x_i}(\tau_{ij} u_i)$	$= \tau_{ij} \frac{\partial u_i}{\partial x_j}$	$+u_j \frac{\partial \tau_{ij}}{\partial x_i}$

An alternative form of the thermal energy equations can be derived by introducing the enthalpy  $h$ .

$$h = e + \frac{p}{\rho} \quad (2.46)$$

$$\frac{Dh}{Dt} = \frac{De}{Dt} + \frac{1}{\rho} \frac{Dp}{Dt} - \frac{p}{\rho^2} \frac{D\rho}{Dt} \quad (2.47)$$

By multiplying this equation with  $\rho$  and inserting equation 2.45 and equation 2.32, this equation can be rewritten into

$$\rho \frac{Dh}{Dt} = -p \underbrace{\frac{\partial u_i}{\partial x_i} + \tau_{ij} \frac{\partial u_i}{\partial x_j} - \frac{\partial q_i}{\partial x_i}}_{\rho \frac{D\varepsilon}{Dt}} + \frac{Dp}{Dt} + p \underbrace{\frac{\partial u_i}{\partial x_i}}_{-\frac{1}{\rho} \frac{D\rho}{Dt}}$$

$$\rho \frac{Dh}{Dt} = \tau_{ij} \frac{\partial u_i}{\partial x_i} + \frac{\partial}{\partial x_i} \left( \kappa \frac{\partial T}{\partial x_i} \right) + \underbrace{\frac{\partial p}{\partial t} + u_i \frac{\partial p}{\partial x_i}}_{\frac{Dp}{Dt}} \quad (2.48)$$

With the definition of the total enthalpy  $H$ , the energy equation can be transformed to

$$H = h + \frac{1}{2} u_i u_i \quad (2.49)$$

$$\rho \frac{DH}{Dt} = \rho \left[ \frac{Dh}{Dt} + \frac{D}{Dt} \left( \frac{1}{2} u_i u_i \right) \right] \quad (2.50)$$

$$\rho \frac{DH}{Dt} = \underbrace{\tau_{ij} \frac{\partial u_j}{\partial x_i} + \frac{\partial}{\partial x_i} \left( \kappa \frac{\partial T}{\partial x_i} \right) + \frac{\partial p}{\partial t} + u_i \frac{\partial p}{\partial x_i}}_{\frac{Dh}{Dt}} + \underbrace{\rho F_i u_i - u_i \frac{\partial \rho}{\partial x_i} + u_i \frac{\partial \tau_{ij}}{\partial x_j}}_{\frac{D}{Dt} \left( \frac{1}{2} u_i u_i \right)} \quad (2.51)$$

$$\rho \frac{DH}{Dt} = \rho F_i u_i + \frac{\partial p}{\partial t} + \frac{\partial}{\partial x_i} (\tau_{ij} u_i) + \frac{\partial}{\partial x_i} \left( \kappa \frac{\partial T}{\partial x_i} \right) \quad (2.52)$$

## 2.5 Navier-Stokes Equation

The momentum equation is rewritten with the help of the euler equation (2.39) and the mass conservation equation (2.32) to

$$\frac{\partial(\rho u_i)}{\partial t} = -\frac{\partial}{\partial x_k} \Pi_{ik} \quad (2.53)$$

where  $\Pi_{ik} = p\delta_{ik} + \rho u_i u_k$  is the specific momentum flux tensor. It is the form of an ideal fluid. A general form can be derived by including  $\tau_{ij}$ .

$$\Pi_{ik} = p\delta_{ik} + \rho u_i u_k - \tau_{ij} \quad (2.54)$$

Inserting the above equation in the momentum equation yields

$$\rho \frac{\partial(u_i)}{\partial t} + u_i \frac{\partial(\rho)}{\partial t} = -\frac{\partial p}{\partial x_i} - \rho u_k \frac{\partial u_i}{\partial x_k} - u_i \frac{\partial(\rho u_k)}{\partial x_k} + \beta \frac{\partial}{\partial x_k} \frac{\partial u_i}{\partial x_k} + \beta \frac{\partial}{\partial x_k} \frac{\partial u_k}{\partial x_i} + \alpha \frac{\partial}{\partial x_i} \frac{\partial u_k}{\partial x_k} \quad (2.55)$$

applying equation 2.32 results in

$$\rho \left( \frac{\partial(u_i)}{\partial t} + u_k \frac{\partial(u_i)}{\partial x_k} \right) = -\frac{\partial p}{\partial x_i} + \beta \nabla^2 u_i + (\alpha + \beta) \frac{\partial^2 u_k}{\partial x_i \partial x_k} \quad (2.56)$$

or in vector form

$$\rho \frac{D\mathbf{u}}{Dt} \equiv \rho \left( \frac{\partial \mathbf{u}}{\partial t} + (\mathbf{u} \nabla) \mathbf{u} \right) = -\nabla p + \beta \nabla^2 \mathbf{u} + (\alpha + \beta) \nabla(\nabla \mathbf{u}) \quad (2.57)$$

which is the most general form of the Navier-Stokes equation [12] [16]. If an Newtonian fluid is considered, equation 2.57 yields

$$\rho \left( \frac{\partial \mathbf{u}}{\partial t} + (\mathbf{u} \nabla) \mathbf{u} \right) = -\nabla p + \beta \nabla^2 \mathbf{u} \quad (2.58)$$

### 2.5.1 Statistical description

The quantities of a turbulent flow  $\phi$  vary randomly at each point. They can be described as mean value  $\langle \phi \rangle$  and fluctuations around the mean  $\delta_\phi$ .

$$\phi = \langle \phi \rangle + \delta_\phi \quad (2.59)$$

The rule for multiplying two quantities is

$$\langle u_i u_k \rangle = \langle (\langle u_i \rangle + \delta_{u_i})(\langle u_k \rangle + \delta_{u_k}) \rangle \quad (2.60)$$

$$\langle u_i u_k \rangle = \langle \langle u_i \rangle \langle u_k \rangle \rangle + \langle \delta_{u_i} \delta_{u_k} \rangle + \langle \langle u_i \rangle \delta_{u_k} \rangle + \langle \langle u_k \rangle \delta_{u_i} \rangle \quad (2.61)$$

$$(2.62)$$

with  $\langle \delta_{u_i} \delta_{u_k} \rangle \neq 0$  and  $\langle \delta_{u_i} \rangle = \langle \delta_{u_k} \rangle = 0$  the previous equation yields

$$\langle u_i u_k \rangle = \langle u_i \rangle \langle u_k \rangle + \langle \delta_{u_i} \delta_{u_k} \rangle \quad (2.63)$$

If the average of the momentum equation (2.54) is taken into account with the help of the equation above, a similar equation as in the absence of turbulence can be derived. The only difference is an additional term  $\rho\langle\delta_{u_i}\delta_{u_k}\rangle$ , which is called the *Reynold stress*.

$$R_{ij} = -\rho\langle\delta_{u_i}\delta_{u_k}\rangle \quad (2.64)$$

This leads to the fact that turbulence can transfer momentum within the fluid like a viscous force.

The Reynolds averaged Navier-Stokes equation reads

$$\boxed{\rho \frac{Du_i}{Dt} = \rho F_i - \frac{\partial p}{\partial x_i} + \frac{\partial(\tau_{ij} - R_{ij})}{\partial x_j}} \quad (2.65)$$

but still contains unknown variables  $\langle\delta_{u_i}\delta_{u_k}\rangle$  as a consequence of averaging. This is called the *Turbulence Closure Problem* because an additional set of algebraic or differential relations is needed to solve this problem.

Mainly, there are two different assumptions for solving this problem. The *Eddy Viscosity / Diffusivity Models* and the *Second-Moment Closure Models*.

The turbulence model of choice for all of the following simulations is the *k - ζ - f Model* which will not be described.

## 2.6 Species Transport Module

This module is used for the calculation of gas mixtures. It solves additional transport equations for each component k of the gas mixture. Those equations can be expressed in the form of

$$\frac{\partial}{\partial t}(\rho\mu_k) + \frac{\partial}{\partial x_i}(\rho u_i \mu_k) = \frac{\partial}{\partial x_i} \left( \Gamma_{\mu_k} \frac{\partial \mu_k}{\partial x_i} + S_{\mu_k} \right) \quad k = 1, \dots, K_{Spe} \quad (2.66)$$

with  $K_{Spe}$  the total number of species and  $\mu_k$  the mass fraction of species k. The diffusion coefficient  $\Gamma_{\mu_k}$  is calculated via

$$\Gamma_{\mu_k} = \left( \rho D_k + \frac{\mu_t}{S_{c_t}} \right) \quad (2.67)$$

with  $D_k$  the diffusion coefficient of species  $k$ , the turbulent viscosity  $\mu_t$  and the turbulent Schmidt number  $S_{ct}$ .

The source term  $S_{\mu_k}$  consists of the reaction rate  $\dot{r}_k$  and the molecular weight  $M_k$  of species  $k$ .

$$S_{\mu_k} = \dot{r}_k M_k \quad (2.68)$$

For the calculation of the molar enthalpy  $H_k$ , the molar entropy  $S_k$  and the molar heat capacity at constant pressure  $C_{pk}$ , the same polynomial approaches are used as stated by the National Aeronautics and Space Administration (NASA) [17]. The approaches are given in the following equations for  $C_{pk}$  and  $H_k$ .

$$\frac{C_{pk}}{R} = a_{1k} + a_{2k}T + a_{3k}T^2 + a_{4k}T^3 + a_{5k}T^4 \quad (2.69)$$

$$\frac{H_k}{RT} = a_{1k} + \frac{a_{2k}}{2}T + \frac{a_{3k}}{3}T^2 + \frac{a_{4k}}{4}T^3 + \frac{a_{5k}}{5}T^4 + \frac{a_{6k}}{T} \quad (2.70)$$

## 2.7 Aftertreatment Module

This module is used in FIRE for simulations related to heat transfer and catalytic reactions. This section gives an introduction how catalytic reactions are treated and how heat conduction is included.

The module can consider a monolith and a packed bed structure of the catalytic material. Since only the packed bed model is used, the monolith model will not be explained.

The modelling of a packed bed reactor is done by a porosity, which contains a solid and a gaseous phase at the same time. The open frontal area (OFA) or void fraction is the ratio between the volume of the gaseous phase and the total volume.

$$OFA = \frac{V_g}{V} \quad (2.71)$$

The flow through the porosity module is simulated by considering pressure losses according to Forchheimer which can be seen in the following equation 2.72.

$$\frac{\partial p}{\partial x_i} = -\alpha_i \mu w_i - \zeta_i \frac{\rho}{2} |w| w_i \quad (2.72)$$

$\frac{\partial p}{\partial x_i}$  is the pressure gradient and is calculated via  $\alpha_i$  the viscous loss coefficient, the dynamic viscosity  $\mu$ , the local velocity in the porosity  $w_i$ , the density of the fluid  $\rho$  and an internal loss coefficient  $\zeta_i$ .

### 2.7.1 Solid energy balance equation

The energy balance equation is calculated by extending Fourier's law.

Fourier's law states that the rate of heat flux  $\dot{Q}$  through a uniform material is directly proportional to the area of heat transfer  $A$  and to the temperature difference  $\Delta T$  in the direction of the heat flux. It is also inversely proportional to the length of the path  $\Delta x$ . The thermal conductivity  $k$  is the constant of proportionality [18].

$$\dot{Q} = -kA \frac{dT}{dx} \quad (2.73)$$

$$q = -k \frac{dT}{dx} \quad (2.74)$$

The energy balance equation can be written as

$$\int_V \dot{E}_\nu \, dV = \int_V k \nabla T + \dot{q}_\nu \, dV \quad (2.75)$$

where

$$\dot{E}_\nu = \rho \cdot c_p \cdot \frac{\partial T}{\partial t} \quad (2.76)$$

is the time rate of change of the internal energy per unit volume and  $\dot{q}_\nu$  is the rate at which energy is generated per unit volume.

FIRE considers anisotropic heat conduction and an additional source term, which leads to

$$\int_{V_s} \rho_s \cdot \frac{\partial(c_{p,s} \cdot T_s)}{\partial t} \cdot dV = \int_{A_s} (\mathbf{K} \nabla T) \cdot \vec{n} \cdot dS + k_h \cdot GSA \cdot V \cdot (T_g - T_s) + S_r \quad (2.77)$$

with

$\mathbf{K}$	...	anisotropic heat conduction matrix
$k_h$	...	gas-solid heat transfer coefficient
$GSA$	...	Geometric surface area
$T_s$	...	solid temperature
$T_g$	...	gas temperature
$S_r$	...	chemical reaction source

It is assumed that the cross stream and stream wise solid thermal conductivities are linearly linked and differ only from an anisotropy factor. The solid heat conduction  $\mathbf{K}$  reads

$$\mathbf{K} = \mathbf{Q}^{-1} \Lambda \mathbf{Q} \quad (2.78)$$

with

$$\Lambda = \begin{pmatrix} \lambda_s & 0 & 0 \\ 0 & G\lambda_s & 0 \\ 0 & 0 & G\lambda_s \end{pmatrix} \quad (2.79)$$

where  $\Lambda$  is the conduction matrix in the catalyst reference frame and  $\mathbf{Q}$  and  $\mathbf{Q}^{-1}$  are the transfer matrices from the catalyst reference frame to the Cartesian reference frame.  $\lambda_s$  is the solid thermal conductivity and  $G$  is the anisotropic conductivity factor.

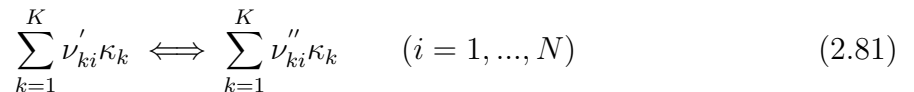
The heat source due to chemical reactions  $S_r$  is calculated by using the species' reaction rates and the corresponding enthalpies of formation.

$$S_r = \sum_{k=1}^K \dot{r}_k H_{fk}|_{298K} V \quad (2.80)$$

$\dot{r}_k$  is the reaction rate of species  $k$   $\left[\frac{\text{kmol}}{\text{m}^3 \text{s}}\right]$  and  $H_{fk}|_{298K}$  is the formation enthalpy of species  $k$  at 298 K.

### 2.7.2 Chemical Reaction Rate Calculation

A chemical reaction can be written in the form given by Coltrin [19]



with

- $\nu', \nu''$  ... stoichiometric coefficients of educts and products
- $\kappa$  ... chemical symbol of the  $k^{\text{th}}$  species
- $K$  ... total number of species
- $N$  ... total number of considered chemical reactions

The stoichiometric coefficient of species  $k$  in reaction  $i$  is defined as

$$\nu_{ki} = \nu'_{ki} - \nu''_{ki} \quad (2.82)$$

and the rate of production of species  $k$  is

$$\dot{r}_k = \sum_{i=1}^N \nu_{ki} \dot{q}_i \quad (2.83)$$

and the reaction rate  $\dot{q}_i$  is defined as the difference between forward and backward reaction rates

$$\dot{q}_i = k_{f_i} \prod_{k=1}^K (c_{k,g})^{F_{0_{ki}}} - k_{r_i} \prod_{k=1}^K (c_{k,g})^{R_{0_{ki}}} \quad (2.84)$$

$F_{0_{ki}}$  and  $R_{0_{ki}}$  are the exponents of concentration of the gas phase species in reaction  $i$ . The definition of  $c_{k,g}$  depends on the phase the species is part of. An ideal gas is assumed for the gas phase

$$c_{k,g} = y_{k,g} \frac{p_g}{RT_g} \quad (2.85)$$

$k_{f_i}$  is the forward reaction rate constant and defined via the Arrhenius equation

$$k_{f_i} = A_i T^{b_i} \exp\left(\frac{-E_i}{RT}\right) \quad (2.86)$$

The backward reaction rate constant  $k_{r_i}$  is zero for irreversible reactions but for reversible reactions, it is calculated with  $k_{f_i}$  and the equilibrium constant  $K_{c_i}$ .

$$k_{r_i} = \frac{k_{f_i}}{K_{c_i}} \quad (2.87)$$

### 2.7.3 Transfer Coefficients

For undirected porosities, the transport coefficients for heat  $k_h$  and the mass of the species  $k_{k,m}$  can be depicted as

$$k_h = \frac{Nu \cdot \lambda_g}{d_{hyd}} \quad (2.88)$$

$$k_{k,m} = \frac{Sh \cdot D_{k,g}}{d_{hyd}} \quad (2.89)$$

with  $Nu$  the Nusselt number,  $Sh$  the Sherwood number,  $\lambda_g$  the thermal conductivity of the gas mixture,  $D_{k,g}$  the diffusion coefficient of species  $k$  in the gas mixture and  $d_{hyd}$  the hydraulic diameter, which represents the characteristic pore length.

The heat transfer coefficient of packed beds with spheres of uniform size is much higher than that of a single sphere, due to the production of vortices, when the fluid flows through the space between the spheres.

The averaged Nusselt number in packed beds is proportional to the Nusselt number of a single sphere [20].

$$Nu = Nu_{sp} \cdot f_\varepsilon \quad (2.90)$$

$f_\varepsilon$  is the shape factor and depends on the fluid volume fraction  $\varepsilon_g$

$$f_\varepsilon = 1 + 1.5(1 - \varepsilon_g) \quad (2.91)$$

The Nusselt number for a sphere is calculated via

$$Nu_{sp} = 2 + \sqrt{Nu_{lam}^2 + Nu_{turb}^2} \quad (2.92)$$

$$Nu_{lam} = 0.664 \cdot \sqrt{Re} \sqrt[3]{Pr} \quad (2.93)$$

$$Nu_{turb} = \frac{0.037 \cdot Re^{0.8} \cdot Pr}{1 + 2.433 \cdot Re^{-0.1} (Pr^{\frac{2}{3}} - 1)} \quad (2.94)$$

If the packed bed consists of non-spherical particles, an equivalent diameter  $d_p$  has to be defined for a sphere with the same surface area as the particle.

The Sherwood number for the mass transfer coefficient can be calculated in the same way as the Nusselt number.

$$\text{Sh}_{sp} = 2 + \sqrt{\text{Sh}_{lam}^2 + \text{Sh}_{turb}^2} \quad (2.95)$$

$$\text{Sh}_{lam} = 0.664 \cdot \sqrt{\text{Re}} \sqrt[3]{\text{Sc}} \quad (2.96)$$

$$\text{Sh}_{turb} = \frac{0.037 \cdot \text{Re}^{0.8} \cdot \text{Sc}}{1 + 2.433 \cdot \text{Re}^{-0.1} (\text{Sc}^{\frac{2}{3}} - 1)} \quad (2.97)$$

The equations were taken from the Aftertreatment Module Manual [18].

## 2.8 Calculation of the Equilibrium Constant

The equilibrium constants are calculated via the Gibbs free energy, which consists of the enthalpy and entropy [21]. For the temperature dependency of the entropy and enthalpy, the specific heat capacities of the investigated temperature has to be included.

The standard reaction enthalpy given by [21] is

$$\Delta_R H_m^0(T^0) = \sum_i \nu_{sti} \Delta_B H_{mi}^0(T^0) \quad (2.98)$$

and the equation for the temperature dependency of the change of enthalpy is

$$\Delta_R H_m^0(T) = \Delta_R H_m^0(T^0) + \sum_i \nu_{sti} \int_{T^0}^T C_{mpi}(T) dT \quad (2.99)$$

The standard reaction entropy is

$$\Delta_R S_m^0(T^0, p^0) = \sum_i \nu_{sti} \Delta_B S_{mi}^0(T^0, p^0) \quad (2.100)$$

and the equation for the temperature dependency of the change of enthalpy is

$$\Delta_R S_m^0(T) = \Delta_R S_m^0(T^0, p^0) + \sum_i \nu_{sti} \int_{T^0}^T \frac{C_{mpi}(T)}{T} dT \quad (2.101)$$

$\nu_{sti}$  are the stoichiometric coefficients.

The heat capacity is modelled with a polynomial approach in the range of 273 K to 1300 K with

$$C_p = a + b \left( \frac{T}{1000} \right) + c \left( \frac{T}{1000} \right)^2 + d \left( \frac{T}{1000} \right)^3 \quad (2.102)$$

The coefficients for the part reactions are depicted in Table 2.1 The values are taken from [22] and were validated in section 4.2.4 by means of Bahin [23, 24]

**Table 2.1:** Coefficients for equation 2.102 to calculate the temperature dependent specific heat capacity for different species. The values are taken from [22].

	a	b	c	d
CH <sub>4</sub>	17.46	60.5	1.118	-7.21
H <sub>2</sub> O	30.38	9.621	1.185	0
CO	27.63	5.024	0	0
CO <sub>2</sub>	21.57	63.74	-40.53	9.684
H <sub>2</sub>	29.09	-0.8347	2.013	0

The binding energy and the entropy for each species is

**Table 2.2:** Binding enthalpy and entropy at standard temperature. The values were taken from [23, 24, 25].

	$\Delta_B H_{mi}^0(T^0) \left[ \frac{J}{mol} \right]$	$\Delta_R S_m^0(T^0, p^0) \left[ \frac{J}{K \cdot mol} \right]$
CH <sub>4</sub>	-75000	186.26
H <sub>2</sub> O	-242000	188.83
CO	-110600	197.67
CO <sub>2</sub>	-394000	213.74
H <sub>2</sub>	0	130.68

It has to be considered that the stoichiometric coefficients ( $\nu_{sti}$ ) for the educts have to be multiplied with -1 and therefore the standard reaction enthalpy has a value of

$$\Delta_R H_m^0(T^0) = 206400 \left[ \frac{J}{mol} \right]$$

and the standard reaction entropy of

$$\Delta_R S_m^0(T^0, p^0) = 214.62 \left[ \frac{J}{K \cdot mol} \right]$$

The Gibbs free energy can be written as:

$$\Delta_R G_m^0(T, p_0) = \Delta_R H_m^0(T) - T \Delta_R S_m^0(T, p^0) \quad (2.103)$$

$$\Delta_R G_m(T, p) = \Delta_R G_m^0(T, p_0) + RT \ln \left( \frac{p}{p_0} \right) \quad (2.104)$$

The condition for chemical equilibrium is  $\Delta_R G_m = 0$ , which results in

$$-\frac{\Delta_R G_m^0(T, p_0)}{RT} = \sum_{i=1}^k \nu_{st \ i} \ln \left( \frac{p}{p_0} \right) = \ln(K_e) \quad (2.105)$$

The equilibrium constant can be written in the form of

$$K_e(T) = \exp \left( \frac{-\Delta_R G_m^0(T, p_0)}{RT} \right) \quad (2.106)$$

which gives the ratio between products and educts at a specific temperature. For standard pressure, the calculation of the equilibrium constant can be simplified to

$$K_e(T) = \frac{\prod_{i=1}^k \nu_{i_p}^{\nu_{st \ i_p}}}{\prod_{i=1}^k \nu_{i_e}^{\nu_{st \ i_e}}} \quad (2.107)$$

For the partial reaction,



$K_e(T)$  is

$$K_e(T) = \frac{\nu_{CO} \nu_{H_2}^3}{\nu_{CH_4} \nu_{H_2O}} \quad (2.109)$$

The equilibrium concentration  $\nu_i$  for each species can be calculated by knowing  $K_e(T)$  via the Gibbs free energy (equation 2.106) and by using the nuclear balance equations, which are now shown for this reaction.

$$\textcircled{1} \quad A_{\text{H}}^{\text{C}} = \frac{\nu_{\text{CH}_4} + \nu_{\text{CO}}}{4\nu_{\text{CH}_4} + 2\nu_{\text{H}_2\text{O}} + 2\nu_{\text{H}_2}} = \frac{1}{6}$$

$$\textcircled{2} \quad A_{\text{H}}^{\text{O}} = \frac{\nu_{\text{H}_2\text{O}} + \nu_{\text{CO}}}{4\nu_{\text{CH}_4} + 2\nu_{\text{H}_2\text{O}} + 2\nu_{\text{H}_2}} = \frac{1}{6}$$

$$\textcircled{3} \quad \sum_i^k \nu_i = 1$$

$$\textcircled{4} \quad K_e(T) = \frac{\nu_{\text{CO}} \cdot \nu_{\text{H}_2}^3}{\nu_{\text{CH}_4} \cdot \nu_{\text{H}_2\text{O}}}$$

Setting  $\textcircled{1}$  equals  $\textcircled{2}$  leads to

$$\nu_{\text{CH}_4} = \nu_{\text{H}_2\text{O}}$$

This result has to be plugged into equation  $\textcircled{1}$  and solved for  $\nu_{\text{H}_2\text{O}}$ . Applying this to  $\textcircled{2}$  results in the solution of the linear equation system which yields

$$\begin{aligned} \nu_{\text{H}_2} &= 3\nu_{\text{CO}} \\ \nu_{\text{CH}_4} &= \frac{1}{2}(1 - 4\nu_{\text{CO}}) \\ \nu_{\text{H}_2\text{O}} &= \frac{1}{2}(1 - 4\nu_{\text{CO}}) \end{aligned} \tag{2.110}$$

This leads to a form of the equilibrium constant which can be solved numerically for  $\nu_{\text{CO}}$  for each temperature step.

$$K_e(T) = \frac{\nu_{\text{CO}} (3\nu_{\text{CO}})^3}{\frac{1}{4}(1 - 4\nu_{\text{CO}})^2} \tag{2.111}$$

The description above is an example for the first partial reaction. The calculation was repeated for the other two partial reaction and the results are shown in the section 4.2.4

# CHAPTER 3

---

## Model and Methods

---

Within the context of this thesis, the focus was on the implementation of a kinetic model for MSR. At first the kinetic, catalytic and geometric parameters of Hoang [6] were used for the development of the model in FIRE. The results were compared to the one given by Hoang [6] in section 4.1. This model is referred to as the benchmark model. After its validation, the geometric and catalytic parameters were changed to the properties of the reformer of interest (Table 3.3). The simulations were compared to measurements done by Somare [26] at AVL. With regard to those results, parameters were changed and recalculated to fit the measurements.

The goal was to develop one kinetic model, that gives reasonable results regardless of the geometric and catalytic parameters.

The following sections state the used parameters for the creation of the model. Section 3.1 depicts the mechanical, geometrical and catalytic parameters for the benchmark and the AVL reformer. Afterwards, the implementation of the reaction kinetics is shown in section 3.2 as well as all equations and parameters concerning the build up of a kinetic model. The used meshes and solver settings can be taken from section 3.3 and section 3.4 gives a brief summary about the used optimization tool.

### 3.1 Catalytic Parameters

The properties of the used reformers are given in the following sections. They differ by its geometry, the used catalytic material and flow and pressure specifications. The values

are essential for the setting of boundary and initial conditions in the simulation, like the pressure specification at the outlet, the mole fractions of the gas concentrations and the mass flow.

### 3.1.1 Settings and Parameters for the Benchmark Model

The geometry specifications and parameters for the benchmarked reformer are given in Table 3.1.

**Table 3.1:** Properties of the reformer of the benchmark model taken from Hoang [6].

Outlet pressure	1.5 bar
Steam to carbon ratio $\frac{S}{C}$	3.5
Residence time $\equiv$ Massflow	3.6 (kg s)/mol $\equiv$ 0.1986 g/s
Length	15 cm
Inner diameter	1 cm
Catalyst loading	8.98 g
Washcoat loading	762 g/l
Open frontal area (OFA) $\equiv$ void fraction	0.35
Particle diameter	1.75 mm
Catalyst density $\rho_{\text{Cat}}$	2.17 g/cm <sup>3</sup>
Specific heat	880 J/(kg K)

To build up a model, other parameters like the hydraulic diameter  $d_{\text{hyd}}$  and the geometric surface area of the catalyst ( $\text{GSA}_{\text{Cat}}$ ) are needed. They are calculated by using the following equation.

$$\text{GSA}_{\text{sphere}} = \frac{3}{r}$$

$$\text{Volume}_{\text{Material}} = (1 - \text{OFA}) \text{Volume}_{\text{Reformer}}$$

$$\text{Inner surface (IS)} = \text{Volume}_{\text{Material}} \text{GSA}_{\text{sphere}}$$

$$\text{GSA}_{\text{Cat}} = \frac{\text{IS}}{\text{Volume}_{\text{Reformer}}}$$

$$d_{\text{hyd}} = 4 \frac{\text{OFA}}{\text{GSA}_{\text{Cat}}} \quad (3.1)$$

This calculation yields

**Table 3.2:** Calculated properties of the benchmark reformer.

$GSA_{\text{Cat}}$	2228.6 $\frac{\text{m}^2}{\text{m}^3}$
$d_{\text{hyd}}$	0.6282 mm

### 3.1.2 Settings and Parameters for the AVL Reformer

The parameters of this reformer were measured by Fasching [27] and Somare [26]. The GSA and the hydraulic diameter were calculated with equation 3.1.

**Table 3.3:** Properties of the AVL reformer. The values were taken with respect to [26, 27].

Outlet pressure	1.2 bar
Steam to carbon ratio $\frac{S}{C}$	2
Massflow	260 g/h
Length	76 cm
Inner diameter	2.97 cm
Catalyst loading	471.6 g
Washcoat loading	890 g/l
Open frontal area (OFA)	0.5
Particle diameter	4.7 mm
Catalyst density $\rho_{\text{Cat}}$	1200 kg/m <sup>3</sup>
$GSA_{\text{Cat}}$	638.3 m <sup>2</sup> /m <sup>3</sup>
$d_{\text{hyd}}$	0.7833 mm
Specific heat	880 J/(kg K)

## 3.2 Reaction Kinetics and Model Development

The kinetic parameters for methane steam reforming (MSR) given in literature vary by a few orders of magnitude [5, 6, 7, 28] (Table 3.5 and Table 4.2). This is due to the fact that those parameters depend on the catalytic properties. Since the paper from Xu and Froment [5], published in 1989, they all have in common that MSR is being described with only three partial reactions.

**Table 3.4:** Governing partial reactions for MSR. The reactions were given by Hoang [6].

No.	Reaction	$\Delta H_{298}$ (kJ/mol)
1	$\text{CH}_4 + \text{H}_2\text{O} \rightleftharpoons \text{CO} + 3\text{H}_2$	206.1
2	$\text{CO} + \text{H}_2\text{O} \rightleftharpoons \text{CO}_2 + \text{H}_2$	-41.15
3	$\text{CH}_4 + 2\text{H}_2\text{O} \rightleftharpoons \text{CO}_2 + 4\text{H}_2$	165.0

The used paper for the benchmark was written by Hoang in 2005 [6]. It was chosen because it was one of very few that contained a whole parameter set, which is essential for the creation of the model in BOOST and FIRE.

Hoang developed his parameters from many measurements, built a 2-D model with the extracted parameters and validated it with his measurements. He came to the same form for the rates of reaction as Xu and Froment, which are shown in equation 3.2 to 3.5.

$R_j$  is the rate of reaction for reaction  $j$  with the unit of  $\left[\frac{\text{kmol}}{\text{kg s}}\right]$  and is depicted in the following equations. The formulas are taken from [6] and the used variables are described in equation 3.6 to equation 3.8

$$R_1 = \frac{\frac{k_1}{p_{\text{H}_2}^{2.5}} \left( p_{\text{CH}_4} p_{\text{H}_2\text{O}} - \frac{p_{\text{H}_2}^3 p_{\text{CO}}}{K_{e1}} \right)}{Q_r^2} \quad (3.2)$$

$$R_2 = \frac{\frac{k_2}{p_{\text{H}_2}} \left( p_{\text{CO}} p_{\text{H}_2\text{O}} - \frac{p_{\text{H}_2} p_{\text{CO}_2}}{K_{e2}} \right)}{Q_r^2} \quad (3.3)$$

$$R_3 = \frac{\frac{k_3}{p_{\text{H}_2}^{3.5}} \left( p_{\text{CH}_4} p_{\text{H}_2\text{O}}^2 - \frac{p_{\text{H}_2}^4 p_{\text{CO}_2}}{K_{e3}} \right)}{Q_r^2} \quad (3.4)$$

$$Q_r^2 = 1 + K_{\text{CO}} p_{\text{CO}} + K_{\text{H}_2} p_{\text{H}_2} + K_{\text{CH}_4} p_{\text{CH}_4} + \frac{K_{\text{H}_2\text{O}} p_{\text{H}_2\text{O}}}{p_{\text{H}_2}} \quad (3.5)$$

The used variables are the kinetic rate constant of equation  $j$  ( $k_j$ ) with its corresponding activation energy  $E_j$  and the adsorption constant of species  $i$  ( $K_i$ ) with its corresponding enthalpy  $\Delta H_i$ . Both are calculated via the Arrhenius approach as described in equation 2.86

$$k_j(T) = k_{0j} \exp\left(-\frac{E_j}{RT}\right) \quad (3.6)$$

$$K_i(T) = K_{0i} \exp\left(-\frac{\Delta H_i}{RT}\right) \quad (3.7)$$

Additionally the equilibrium constants  $K_{ej}$  are used. The unit of  $K_{ej}$  is chosen to cancel out the unit of pressure in equation 3.2 to 3.5 with the help of Table 3.5 and Table 3.6.

$$K_{e1} = 5.75 \cdot 10^{12} \exp\left(-\frac{11500}{T}\right) [\text{bar}^2]$$

$$K_{e2} = 1.26 \cdot 10^{-2} \exp\left(\frac{4600}{T}\right)$$

$$K_{e3} = 7.24 \cdot 10^{10} \exp\left(-\frac{21600}{T}\right) [\text{bar}^2] \quad (3.8)$$

The pre-exponential factors for  $k_{0j}$  and  $K_{0i}$  (equation 3.6) and 3.7) are depicted in Table (3.5) and(3.6):

**Table 3.5:** Pre-exponential factors for kinetic rate constants [6]

Reaction	$k_{0j}$ (mol/kg s)	$E_j$ (J/mol)
1	$9.048 \cdot 10^{11} \text{ bar}^{0.5}$	209500
2	$5.43 \cdot 10^5 \text{ bar}^{-1}$	70200
3	$2.14 \cdot 10^9 \text{ bar}^{0.5}$	211500

**Table 3.6:** Pre-exponential factors for adsorption constant [6]

Species	$K_{0i}$ ( $\text{bar}^{-1}$ )	$\Delta H_i$ (J/mol)
CH <sub>4</sub>	$1.995 \cdot 10^{-3}$	-36650
CO	$8.11 \cdot 10^{-5}$	-70230
H <sub>2</sub>	$7.05 \cdot 10^{-9}$	-82550
H <sub>2</sub> O	$1.68 \cdot 10^4 \text{ bar}$	85770

The pre-exponential factors of Table 3.5 are scaling factors for the velocity of the reaction and depend on the catalytic properties like the loading of the catalyst, its reactive surface and the OFA.

### 3.2.1 Implementation of the Kinetic Model

The parameters and equations mentioned in the previous section were implemented in BOOST and FIRE with the AVL user coding interface (AUCI). Additional things had to be considered to ensure convergence and correct calculation.

If the partial pressure of two species of one of the equations 3.2 to 3.4 becomes negative at the same time, which is numerically possible, they could cancel out and the solver would not notice the difference, which could lead to a diverging simulation. This issue was fixed by multiplying an appropriate sign if this condition comes true.

Another problem that had to be faced was the non-integer exponents of  $R_1$  and  $R_3$  (equation 3.2 and 3.4) because negative values for the partial pressure of  $H_2$  would lead to a not-a-number error. This problem is fixed with a logical sign operator, which is described in Figure 3.1. Additionally those functions (for example  $1/p_{H_2}^{2.5}$ ) have a very large gradient in the low concentration region and a singularity at zero, which results in slow convergence or even a diverging simulation. A possibility to get rid of this issue is to make the exponents approach the value one below a specified concentration. The AUCI function that accomplishes this is called *modifyExponent* and uses following polynomial function:

$$n_{mod}(x) = \frac{1-n}{b^p} x^p + n \quad (3.9)$$

with the concentration  $x$ , the original exponent  $n$ , the polynomial order  $p$  and the boundary condition  $b$ , which is the upper boundary value of the concentration for the start of the modification of the exponent.

An example of the implementation is shown in Figure 3.1.

```

1  Reaction rate constant
2  k1 = A_k1 * exp(-E_k1/RT);
3  ke1 = preexp_k1*exp(dH_k1/Ts); ← Equilibrium constant
4
5  d_sign = (P_CH4 < 0.0) || (P_H2O < 0.0) ? -1.0 : 1.0; ← Sign operator for
6  d_sign2 = (P_H2 < 0.0) || (P_CO < 0.0) ? 0.0 : 1.0; ← reaction direction
7
8  d_ord_H2_mod = modifyExponent(P_H2, 0.5, d_boundary, 4); ← Due to singularity
9
10 P_H2_mod05 = pow(fabs(P_H2), d_ord_H2_mod);
11 P_H2_mod25 = pow(max(P_H2, lim),2.5); ← mol -> kmol
12
13 rate = k1* (d_sign * fabs(P_CH4 * P_H2O)/P_H2_mod25 - d_sign2 * P_H2_mod05 * fabs(P_CO)/ke1) / DEN2 / 1000.0;
14 Rate equation

```

Figure 3.1: Part of the AUCI model for  $R_1$  of Table ??

The value  $d\_boundary$  was specified as 0.001.

### 3.3 Mesh and Solver Settings

This section shows the mesh-geometries and solver settings. The first section shows the settings for the literature benchmark model and the second section the settings for the AVL reformer model. It is depicted how the different meshes for fluid and solid are

combined and where selections for the evaluation of the simulations are placed.

### 3.3.1 Benchmark Model

The meshes for the benchmark model were created with the AVL meshing tool "FAME Meshing". The simulation of heat transfer through a solid into a fluid requires two meshes. One for the solid case, which represents the steel tube in which the fluid flows, and one for the fluid case. The coupling of those two cases was done via the "AVL Case Coupling Interface (ACCI)".

Both meshes consist of 80000 cells and have a total length of 0.2 m and an inner diameter of 0.01 m, which include an inlet and an outlet zone (green and red parts of Figure 3.2).

For a more precise analysis, 2-D cell selections were created in which mean values of gas temperature and mole fraction were calculated. The labels of these selections can be seen in Figure 3.2.

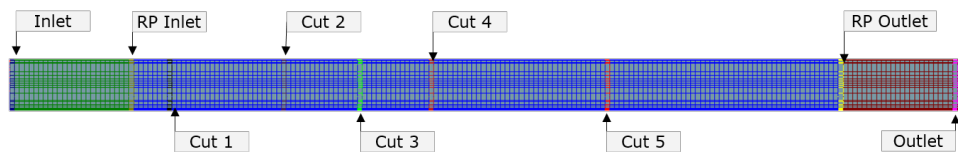


**Figure 3.2:** Mesh of the fluid case of the benchmark model with positions of cuts that are used for mean calculations of mole fractions and gas temperature. "RP inlet" and "RP outlet" indicate the boundaries for the reactive porosity, whereas Cut 1 to 5 are distributed to gain a maximum of information about the dynamic of the reactions. This is due to the fact that the reaction is very fast and most of the reformation takes place in the first half of the reactive porosity.

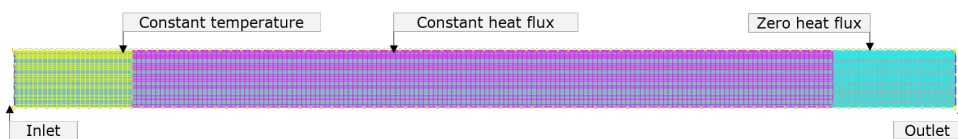


**Figure 3.3:** Mesh of the solid case of the benchmark model with positions of different heat settings

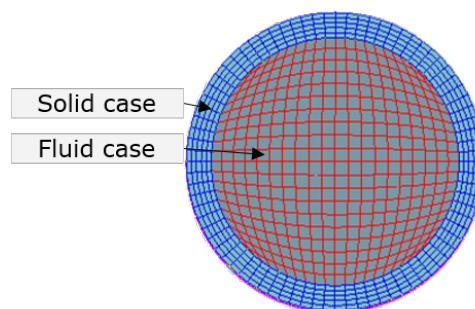


**Figure 3.4:** Meshes of coupled solid and fluid case of the benchmark model

Table 3.7 shows the underrelaxation factors for both cases. The solid case has no factor for species transport. Underrelaxation is described in section 2.2.1.

**Table 3.7:** Underrelaxation factors

Momentum	0.8
Pressure	0.2
Turb. kin. energy	0.6
Turb. diss. rate	0.6
Energy	0.9
Mass source	1.0
Viscosity	1.0
Scalar	1.0
Species transport equation	1.0

A standard model (k- $\zeta$ -f model) was used as turbulence model in the fluid case, as for the solid case, a Laminar model was chosen. Both models are predefined models and are not explained within this thesis. The convergence criteria for normalized residuals are shown in Table 3.8

**Table 3.8:** Convergence criteria

Momentum	1e-04
Pressure	1e-04
Turb. kin. energy	1e-04
Turb. diss. rate	1e-04
Energy	1e-06
Scalar	1e-05

Mass and heat transfer in the reactive porosity (RP) were calculated with the "VDI packed bed" model, developed by "Verein Deutscher Ingenieure" [29] and the pressure drop with "Forchheimer" (see section 2.7)

The solid case corresponds to 1.4841 steel whose properties are given in the following Table 3.9.

**Table 3.9:** Solid case properties for the simulation of the heatflux through the wall of a steel tube

Specific heat	$500 \frac{J}{kg K}$
Thermal conductivity	$15 \frac{W}{m K}$
Reference density	$7.9 \frac{kg}{dm^3}$

### 3.3.2 AVL reformer model

The meshes for the AVL reformer model were created with the same meshing tool as the previous model. Both meshes have 300000 cells, a total length of 0.9 m and an inner diameter of 0.0297 m. The inlet and outlet region is included in the mesh. The positions for the 2-D mean analysis is depicted in Figure 3.5.

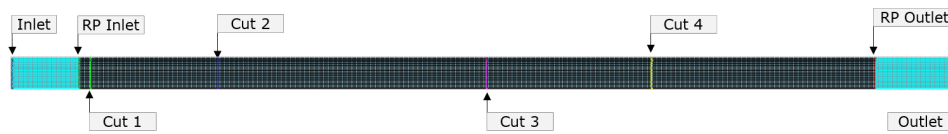


**Figure 3.5:** Mesh of the fluid case of the AVL reformer model with positions of cuts. "RP inlet" and "RP outlet" indicate the boundaries for the reactive porosity, whereas Cut 1 to 4 are distributed in a way that gives much information about the dynamic of the reactions. This is due to the fact that the reaction is very fast and most of the reformation takes place in the first half of the reactive porosity.

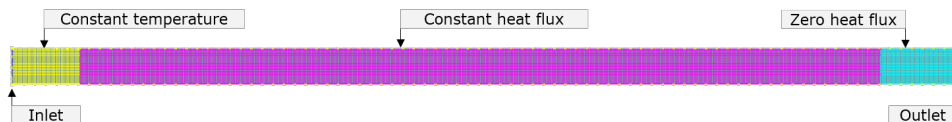


**Figure 3.6:** Mesh of the solid case of the AVL reformer model with positions of different heat settings

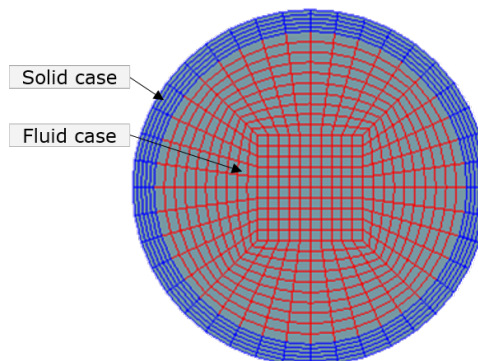


**Figure 3.7:** Meshes of coupled solid and fluid case of the AVL reformer model

Table 3.10 shows the underrelaxation factors for both cases. The solid case has no factor for species transport.

**Table 3.10:** underrelaxation factors for the simulation of the AVL reformer mode

Momentum	0.6
Pressure	0.1
Turb. kin. energy	0.4
Turb. diss. rate	0.4
Energy	0.8
Mass source	0.8
Viscosity	0.8
Scalar	0.8
Species transport equation	0.8

The convergence criteria are the same as in Table Table 3.8 and the pressure drop is calculated with "Forchheimer" (see section 2.7).

The different mesh for the fluid case compared with the benchmark model is due to faster convergence because neighbouring cells with the same geometry are preferred since transmitted values do not have to extrapolated.

Values for the properties of the solid case can be seen in Table 3.9.

### 3.4 Optimization settings

The AVL optimization tool *Design Explorer* was used to optimize the kinetic parameters with regard to the expected outlet gas concentration. The response function was defined as the minimum CH<sub>4</sub> and H<sub>2</sub>O concentration at the outlet and the maximum H<sub>2</sub> concentration at the outlet. The consideration of the other species fraction lead to longer calculations and no improvement of the results.

The optimization was done for the activation energies, the preexponential factors  $k_{0j}$  and both together, but only the optimization for the activation energies led to logical results.

The results are shown in section 4.2.3.

The used algorithm for the optimization was NLPQL and is known in literature (see Schittkowski [30]).

## Results and Discussion

For the validation of the models, the mean gas concentration and the corresponding mean temperature at specific cuts (see Figure 3.2 and Figure 3.5) were compared to equilibrium concentration, calculated with a Gibbs reactor in MATLAB.

The distribution of the equilibrium concentration for MSR was calculated for a temperature range from 0 °C to 1200 °C in MATLAB and compared with literature in Figure 4.1.

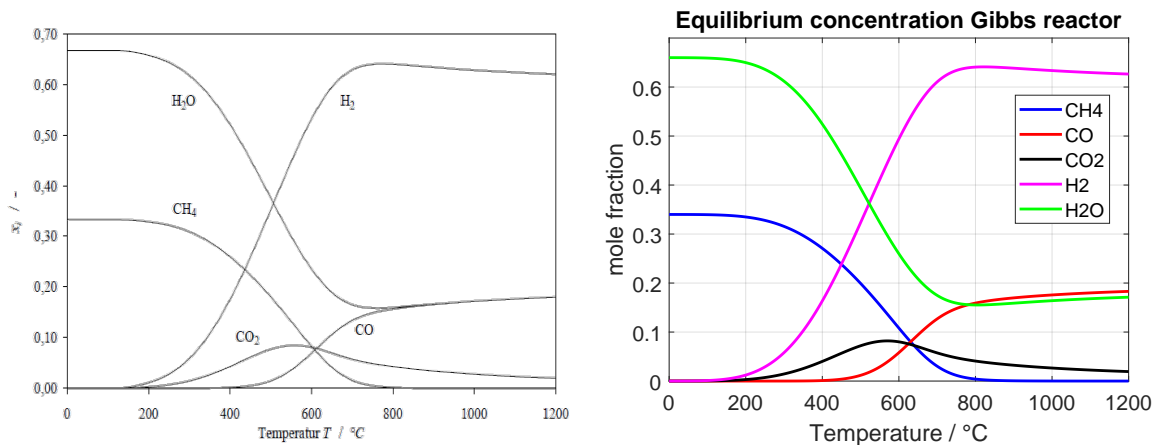


**Figure 4.1:** Validation of the Gibbs reactor. The left figure is taken from Leinfelder[31] and shows the equilibrium concentration dependency of the temperature. The right one depicts the results of the simulation in MATLAB

Section 4.1 compares the outcome of the benchmarked model with the results given in the corresponding literature. It depicts the limitations of the 1-D simulation software and checks it against the results gained from FIRE. The following three sections analyse the results of the AVL reformer model with different sets of kinetic parameters. In section

4.2.4 it is shown, how the change of the equilibrium constant influences the outcome of the simulation, which is further investigated in the last sections of this chapter.

## 4.1 Literature benchmark

The model for Hoang's reformer was first investigated in the 1-D AVL simulation software BOOST. Figure 4.2 shows the species conversion within the reformer given by Hoang[6], while Figure 4.3 and Figure 4.4 show the simulated species concentration over the reactor length in BOOST for two different values of the specific heat. The very large value of 3000 kJ/(kg K) for the specific heat reformer material was used to compensate the temperature loss during the chemical reactions and therefore increase the speed of the reformation since it was not possible to specify an external heat flux in BOOST.

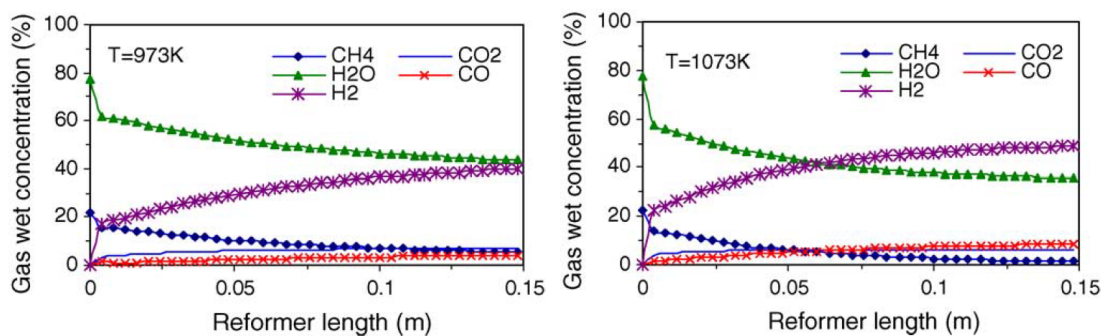


**Figure 4.2:** Changing gas concentration over the reactor length for 973 K (left) and 1073 K (right). The figures were taken from Hoang [6].

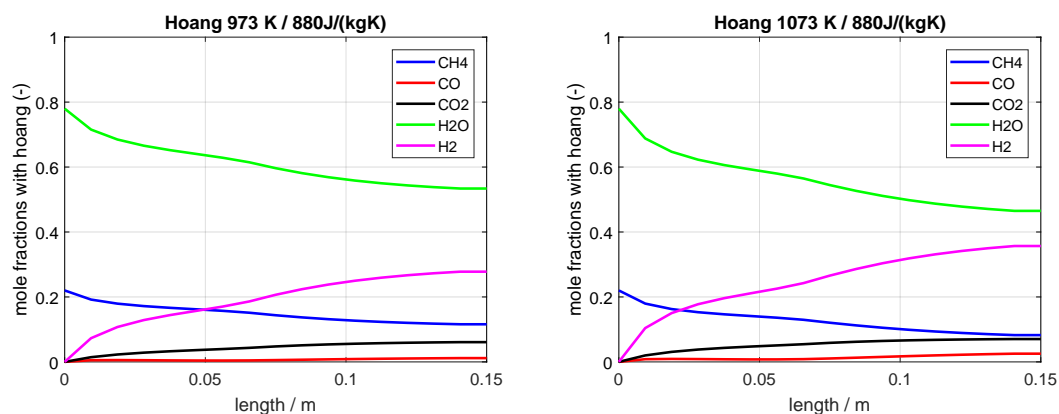


**Figure 4.3:** BOOST results for different temperatures with a specific heat of 880 J/(kg K). The left figure shows the gas concentration with respect to the reactor length at 973 K and the right figure at 1073 K.

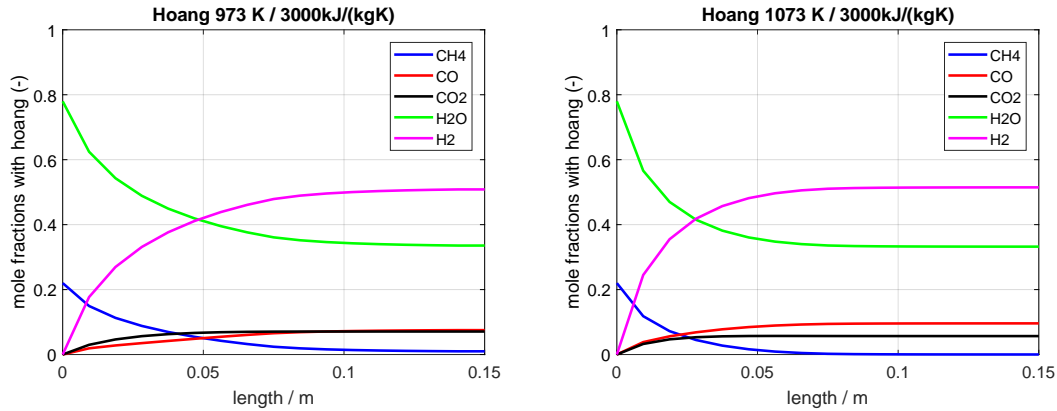


**Figure 4.4:** BOOST results for different temperatures with a specific heat of 3000 kJ/(kg K) The left figure shows the gas concentration with respect to the reactor length at 973 K and the right figure at 1073 K.

The heatflux for the 3-D simulation in FIRE was chosen with regard to Kuroki [8] who specified a heatflux of 60 kW/m<sup>2</sup> for an inlet gas temperature of 973 K and 85 kW/m<sup>2</sup> for an inlet gas temperature of 1073 K. Those heat fluxes are necessary to reach the inlet gas temperature at the outlet, which was achieved in the measurements of Hoang. The region, where the heat flux is applied, is shown in Figure 3.3. The results are depicted in Figure 4.5 to Figure 4.7.

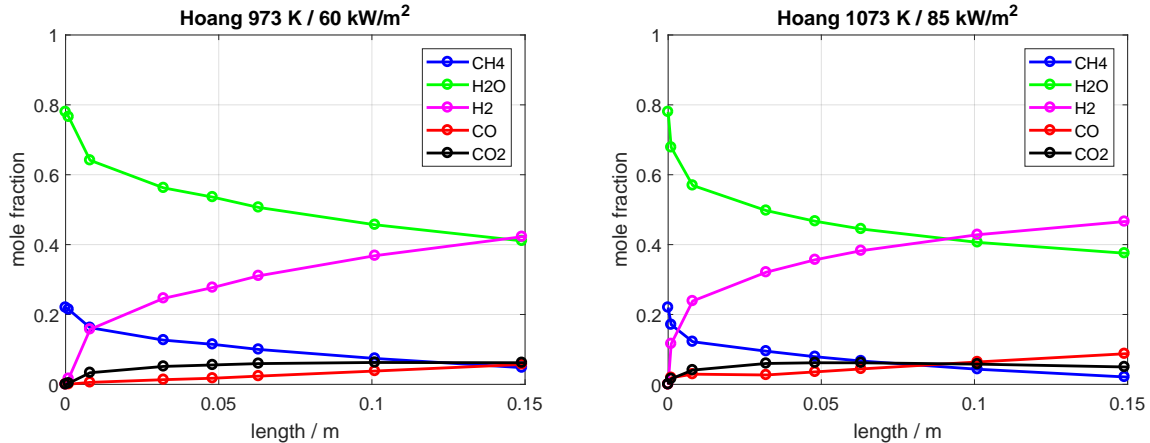


**Figure 4.5:** Mean species concentration at specific cuts of the reformer calculated with FIRE at 973 K with 60 kW/m<sup>2</sup> and 1073 K with 85 kW/m<sup>2</sup>. The position of the cuts in the mesh is shown in Figure 3.2.

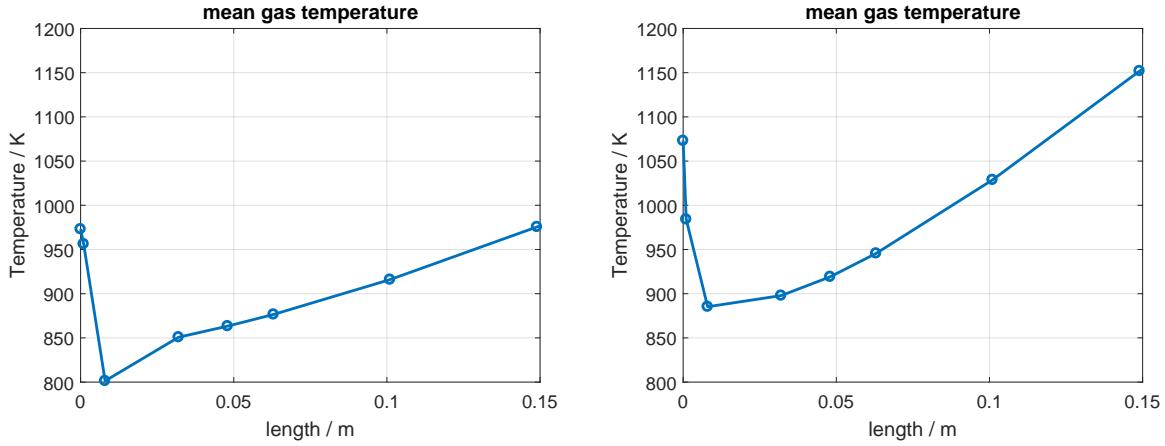


**Figure 4.6:** Mean gas temperature at specific cuts of the reformer calculated with FIRE at 973 K with 60 kW/m<sup>2</sup> and 1073 K with 85 kW/m<sup>2</sup>. The position of the cuts in the mesh is shown in Figure 3.2.

The right diagram in Figure 4.6 shows that the value for the heat flux given by Kuroki for the higher temperature set-point, leads to an overshooting of the outlet gas temperature. This could be due to different models of the reactive porosities or the calculation of the material properties for the heat transfer.

Figure 4.7 compares the results of the simulation over the reformer length with the calculated equilibrium concentration. The temperatures for the calculations were taken from Figure 4.6. It depicts that the simulation does not reach the equilibrium concentration, which can be explained by the short reformer length of 15 cm. It can also be seen that the deviation from the equilibrium at the outlet is smaller for higher temperatures, due to the fact that the speed of the reaction is proportional to the temperature in this temperature region and leads to faster conversion.

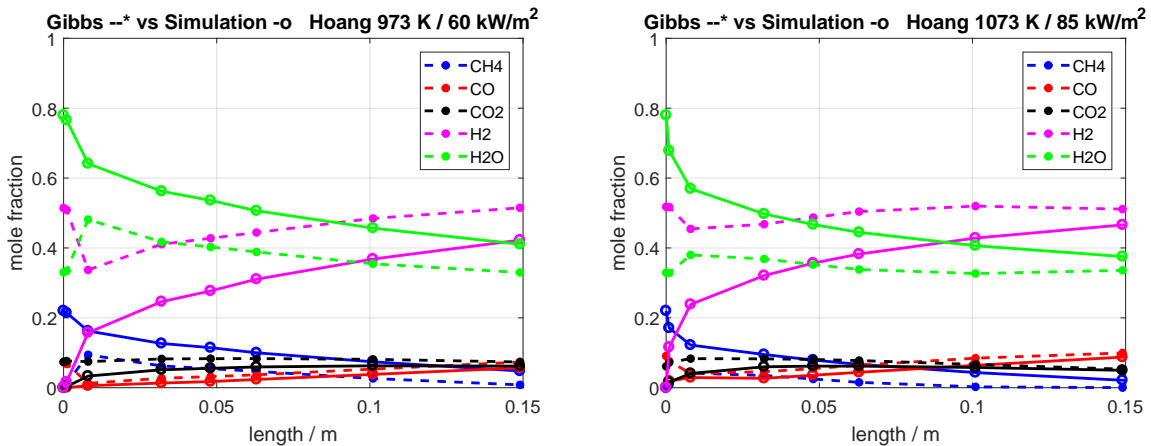


**Figure 4.7:** Mean species concentration calculated with FIRE at 973 K with 60 kW/m<sup>2</sup> and 1073 K with 85 kW/m<sup>2</sup> and Gibbs equilibrium concentration at specific cuts of the reformer. The position of the cuts in the mesh is shown in Figure 3.2.

## 4.2 AVL reformer

The results of the simulation for the model of the AVL reformer (see chapter 3) are shown in this section. At first, all kinetic parameters were taken from Hoang (see Table 3.5 and 3.6) and afterwards modified to investigate their influence and dependency.

The measured gas concentration by Somare [26] is equal to the equilibrium concentration calculated with the Gibbs reactor and is given in Table 4.1.

**Table 4.1:** Measured gas concentration by Somare [26]

Species	mole fraction [%]
CH <sub>4</sub>	15.5
H <sub>2</sub> O	32.4
H <sub>2</sub>	41.1
CO	2.9
CO <sub>2</sub>	8.1

The following figures compare the simulated gas flow temperature along the tube's symmetry axis (Polyline with  $x=0$ ,  $y=0$ ,  $z=[-0.45,0.45]$ ) for different kinetic parameters and heat fluxes with the measured data and the simulated outlet concentration with the measured values .

### 4.2.1 Reaction kinetic parameters of Hoang

Figure 4.8 and Figure 4.9 show the results for a heat flux of  $1000 \text{ W/m}^2$  and  $5000 \text{ W/m}^2$  for the kinetic parameters of Hoang. The region, where the heat flux is applied, is shown in Figure 3.6.  $1000 \text{ W/m}^2$  is the mean heat flux for the same simulation with a constant solid wall temperature of  $818 \text{ K}$ . Since the outlet gas temperature differs by approximately  $30 \text{ K}$  from the measurement, the heat flux was arbitrary increased to  $5000 \text{ W/m}^2$ , which led to an even higher temperature at the outlet compared to the measurement. The mole fractions for CH<sub>4</sub> and H<sub>2</sub>O decrease with increasing temperature which is physically expected. On the other hand, the comparison of the mean gas concentration for specific cuts at a mean temperature with the corresponding equilibrium concentration at this temperature in Figure 4.10 shows a huge discrepancy.

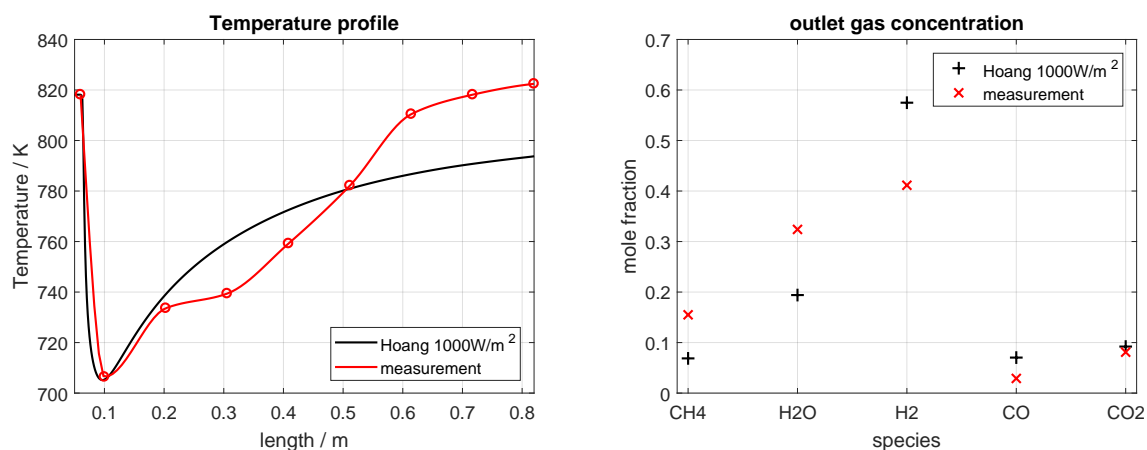


**Figure 4.8:** Comparison of simulated and measured values for Hoang's kinetics and 1000 W/m<sup>2</sup>. The left figure compares the polyline results for the flow temperature with the measurement. The right figure shows the deviation of the simulated mean outlet concentration from the measurement by Somare.

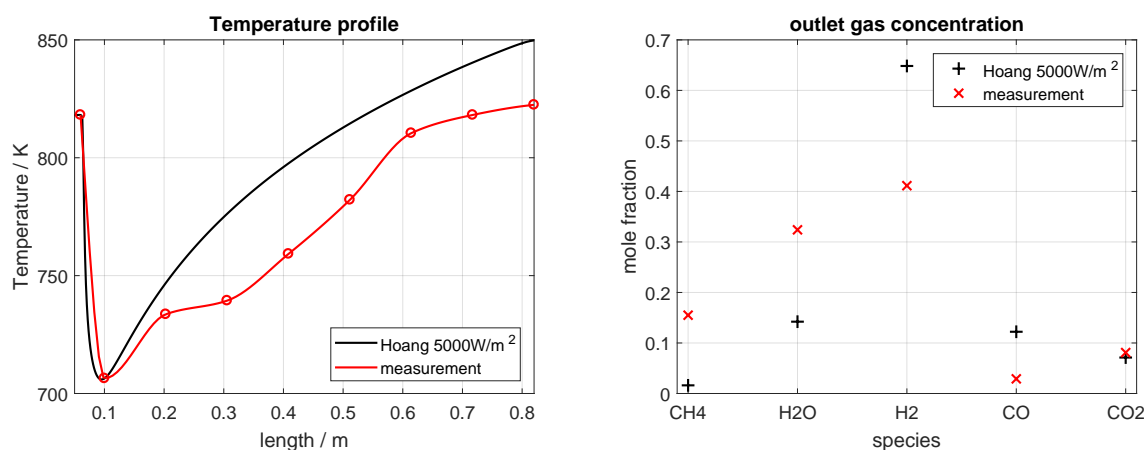


**Figure 4.9:** Comparison of simulated and measured values for Hoang's kinetics and 5000 W/m<sup>2</sup>. The left figure compares the polyline results for the flow temperature with the measurement. The right figure shows the deviation of the simulated mean outlet concentration from the measurement by Somare.

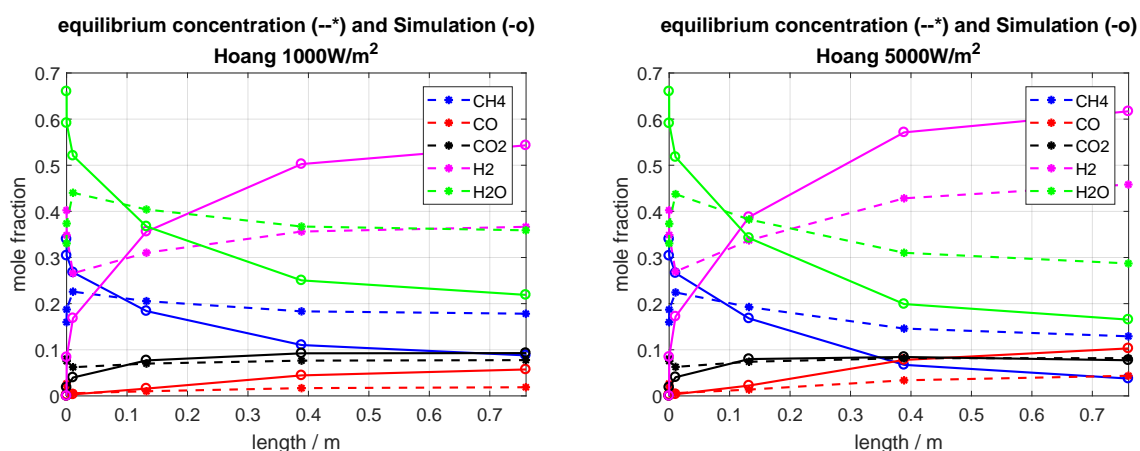


**Figure 4.10:** Comparison of simulation and equilibrium concentration for 1000 W/m<sup>2</sup> and 5000 W/m<sup>2</sup>. The equilibrium concentration was calculated with the Gibbs reactor in MATLAB.

Due to this discrepancy, the kinetic model is not fit for further use and has to be modified.

#### 4.2.2 Reaction Kinetic Parameters of Xu

The same model was used as before but with the pre-exponential factors and activation energies of Xu [5], which are illustrated in Table 4.2.

**Table 4.2:** Pre-exponential factors and activation energies of Xu [5] for the rate of reaction in equation 3.2 to 3.5.

Reaction	$k_{0j}$ (mol/kg s)	$E_j$ (J/mol)
1	$1.167 \cdot 10^{15} \text{ bar}^{0.5}$	240100
2	$1.508 \cdot 10^5 \text{ bar}^{-1}$	67130
3	$2.830 \cdot 10^{14} \text{ bar}^{0.5}$	243900

Figure 4.11 and Figure 4.12 show the results for a heat flux of  $1000 \text{ W/m}^2$  and  $5000 \text{ W/m}^2$  for the kinetic parameters of Xu. This simulations show a trade-off between a smaller deviation of the mole fractions from the measurement but a higher discrepancy in the temperature profile. It can be said that this set of parameters lead to no significant improvement of the simulation.

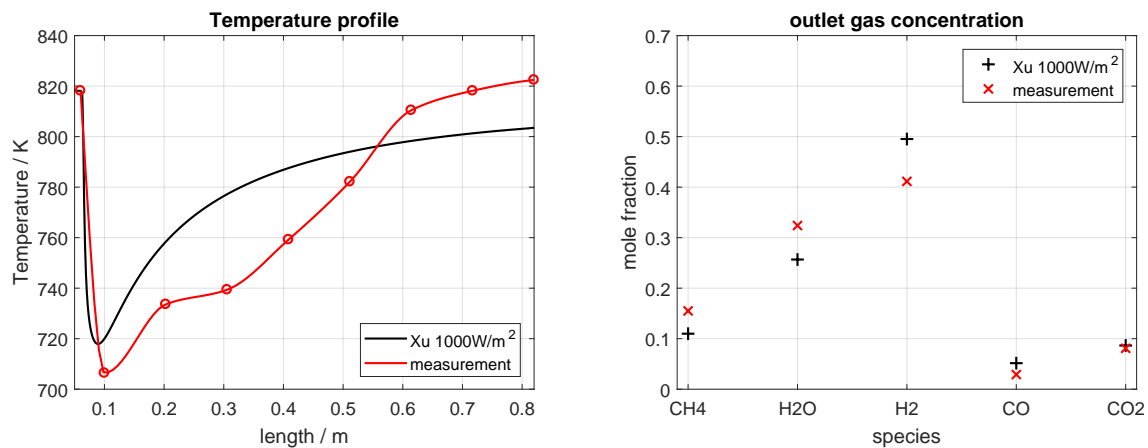


**Figure 4.11:** Comparison of simulated and measured values for Xu's kinetics and  $1000 \text{ W/m}^2$ . The left figure compares the polyline results for the flow temperature with the measurement. The right figure shows the deviation of the simulated mean outlet concentration from the measurement.

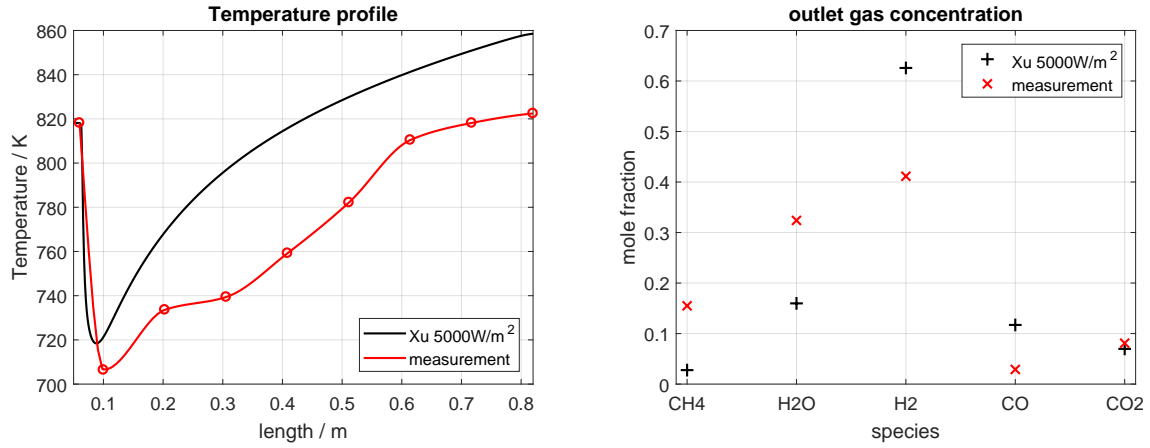


**Figure 4.12:** Comparison of simulated and measured values for Xu's kinetics and  $5000 \text{ W/m}^2$ . The left figure compares the polyline results for the flow temperature with the measurement. The right figure shows the deviation of the simulated mean outlet concentration from the measurement.

The comparison of the mean gas concentration for specific cuts and its mean temperature with the corresponding equilibrium concentration at this temperature, shows also a huge discrepancy.

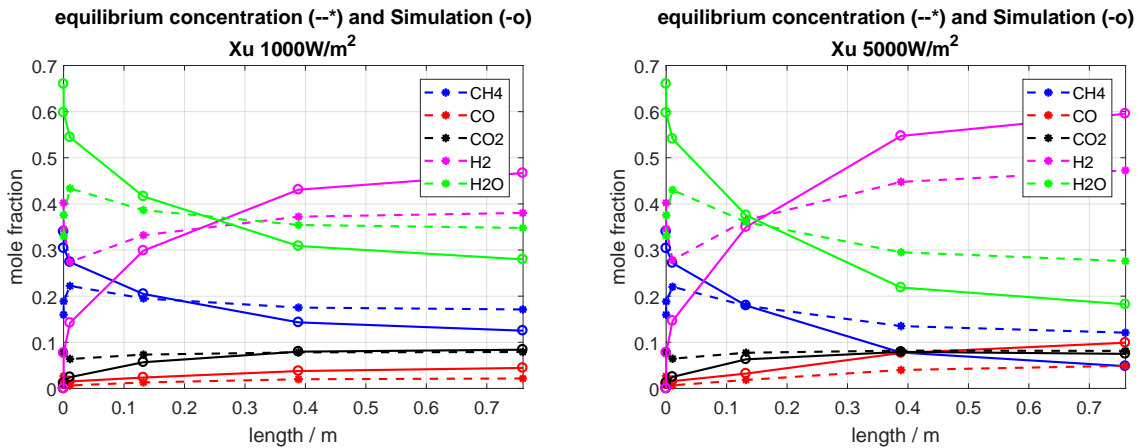


**Figure 4.13:** Comparison of simulation and equilibrium concentration for  $1000 \text{ W/m}^2$  and  $5000 \text{ W/m}^2$ . The equilibrium concentration was calculated with the Gibbs reactor in MATLAB.

### 4.2.3 Optimized activation energies $E_i$

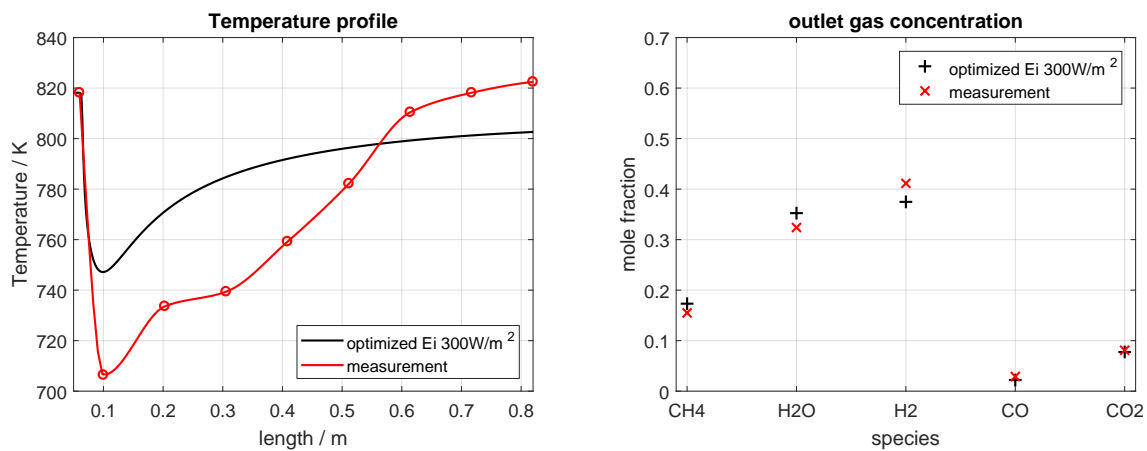
Due to the fact that the expected outlet concentration could not be reached, an optimization algorithm based on the NLPQL method was used in the 1-D simulation tool BOOST. The start values for the optimization were the kinetic parameters of Hoang and the optimum activation energies with this method are shown in the following Table 4.3. The optimization was also done for the pre-exponential factors and the pre-exponential factors plus the activation energies, but both optimizations led to non-physical values for

the pre-exponential factors. Therefore they are not shown in this section.

**Table 4.3:** Pre-exponential factors of Hoang and optimized activation energies

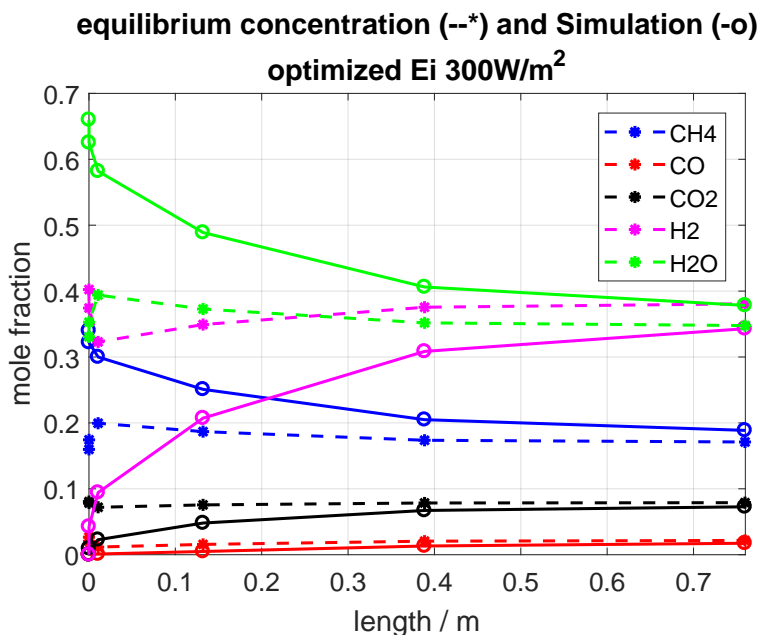
Reaction	$k_{0j}$ (mol/kg s)	$E_j$ (J/mol)
1	$9.048 \cdot 10^{11} \text{ bar}^{0.5}$	232772
2	$5.43 \cdot 10^5 \text{ bar}^{-1}$	73057
3	$2.14 \cdot 10^9 \text{ bar}^{0.5}$	221815

Figure 4.14 compares the measured values with the results of the simulation with optimized activation energies.



**Figure 4.14:** Comparison of simulated and measured values for the optimized activation energies and  $300 \text{ W/m}^2$ . The left figure compares the polyline results for the flow temperature with the measurement. The right figure shows the derivation of the simulated mean outlet concentration from the measurement.

Figure 4.15 shows that the equilibrium concentration can be reached in contrast to the previous simulation, but the temperature profile differs much more. The reason for this result is, that the optimization was not done with regard to an external heat flux, which was not possible in BOOST.

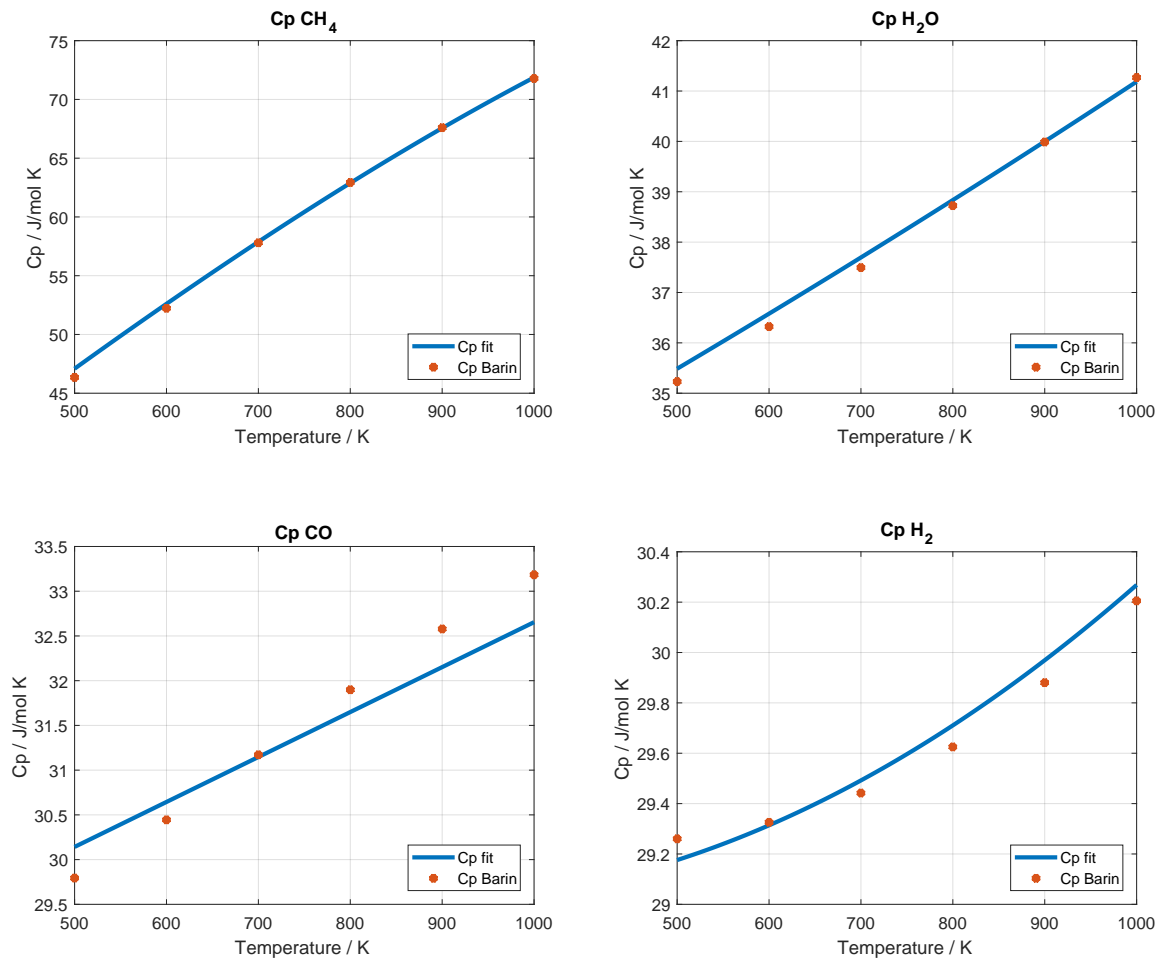


**Figure 4.15:** Comparison of simulation with optimized activation energies and equilibrium concentration for 300 W/m<sup>2</sup>. The equilibrium concentration was calculated with the Gibbs reactor in MATLAB

#### 4.2.4 Equilibrium constant

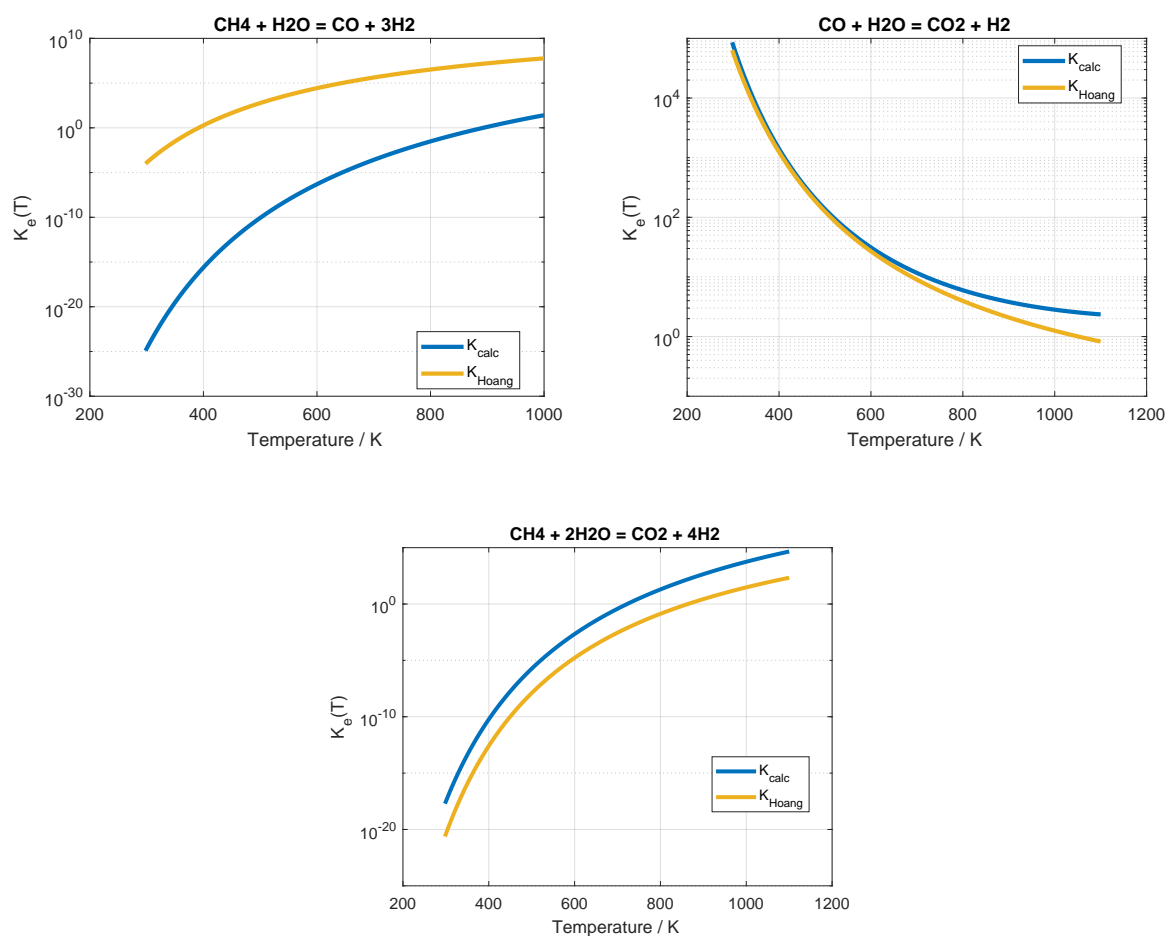
The previous results show, that either the temperature profile fits the measured data and the concentration differs from the expected value or the other way around. Since the variation of the kinetic parameters lead to no satisfying result, the equilibrium functions of each partial reactions were investigated as described in the section 2.8.

The function for the specific heat capacity (equation 2.102) with the values given in Table 2.1 is depicted in Figure 4.17. This figure shows, that the deviation of the function from the values stated by Barin [23, 24] is negligible. Therefore equation 2.102 is used for the calculation of the specific heat capacity.



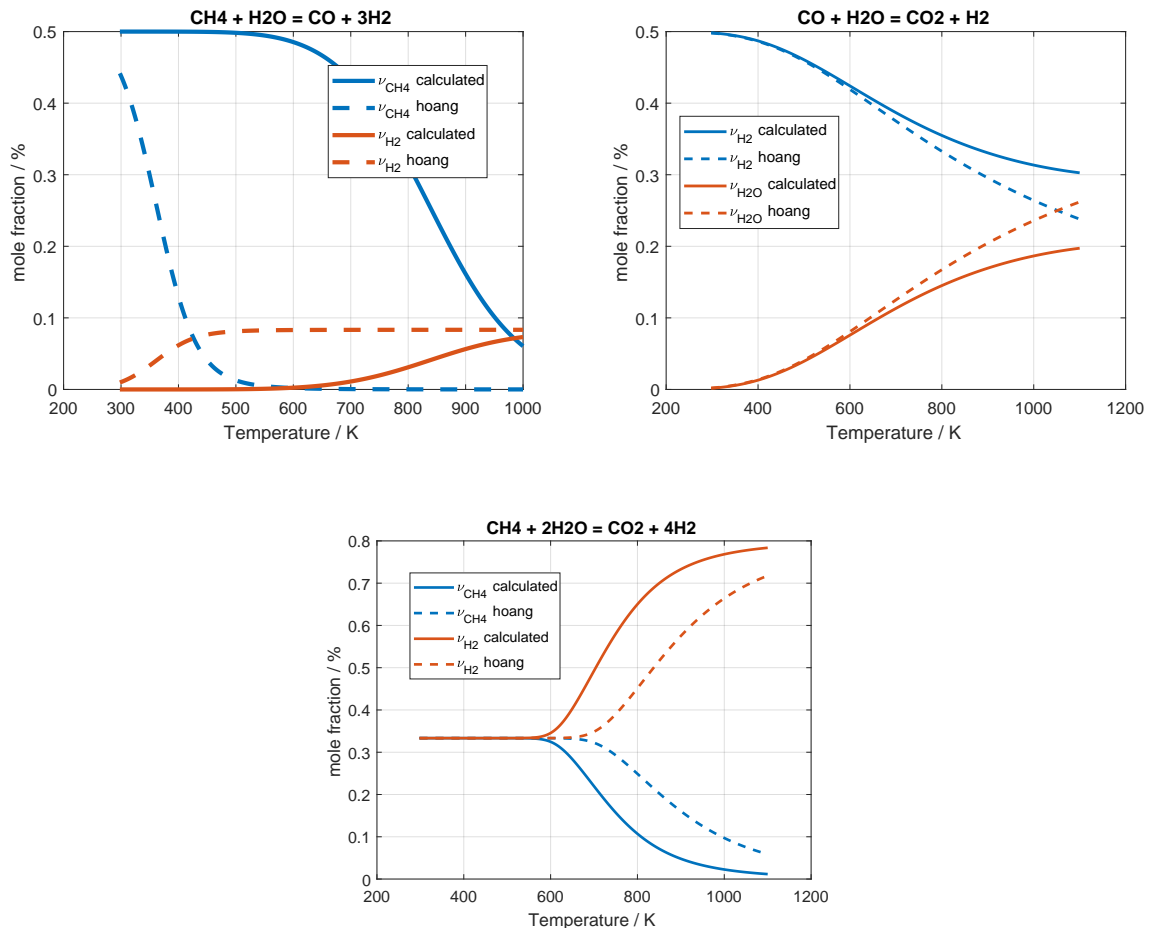
**Figure 4.17:** Comparison between the values for the specific heat capacity given by Barin [23, 24] and the calculated values with equation 2.102 and the coefficients of Table 2.1

Figure 4.19 shows the calculated equilibrium constants and compares them to the ones used by Hoang. It can be seen that the equilibrium constant used by Hoang differ by more than seven orders of magnitude from the calculated one. This explains the overshooting of the equilibrium concentration in the previous simulations.



**Figure 4.19:** Equilibrium constants for all three partial reactions. The blue line ( $K_{calc}$ ) refers to the calculated equilibrium constant in section 2.8. The yellow line ( $K_{Hoang}$ ) refers to the functions given in equation 3.8

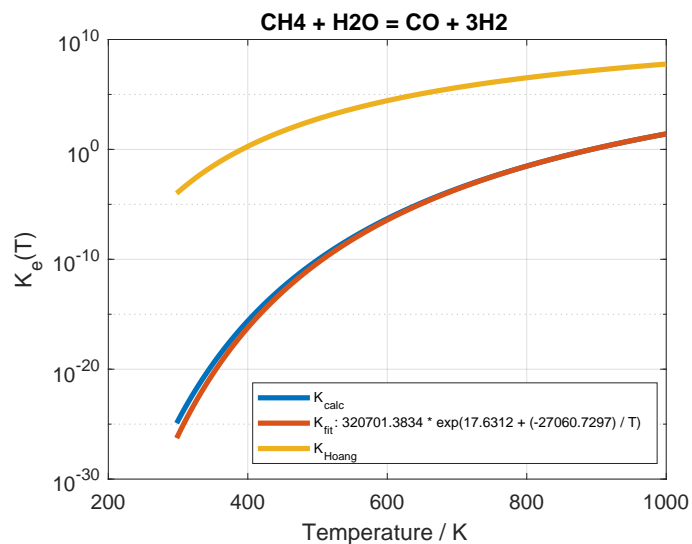
Figure 4.21 shows the  $\text{CH}_4$  and  $\text{H}_2$  concentration calculated with regard to equation 2.110 for each equilibrium constant and compares them to the ones mentioned in equation 3.8. The first diagram shows a too fast methane conversion for Hoang's setting (dotted blue line) at a temperature range, where nearly no reforming should take place (solid blue line). All other diagrams show a reasonable behaviour.



**Figure 4.21:** Mole fractions calculated for each equilibrium constant for all three partial reactions. The dotted lines corresponds to the equilibrium constants of Hoang given in equation 3.8 and the continuous lines to the calculated equilibrium constants.

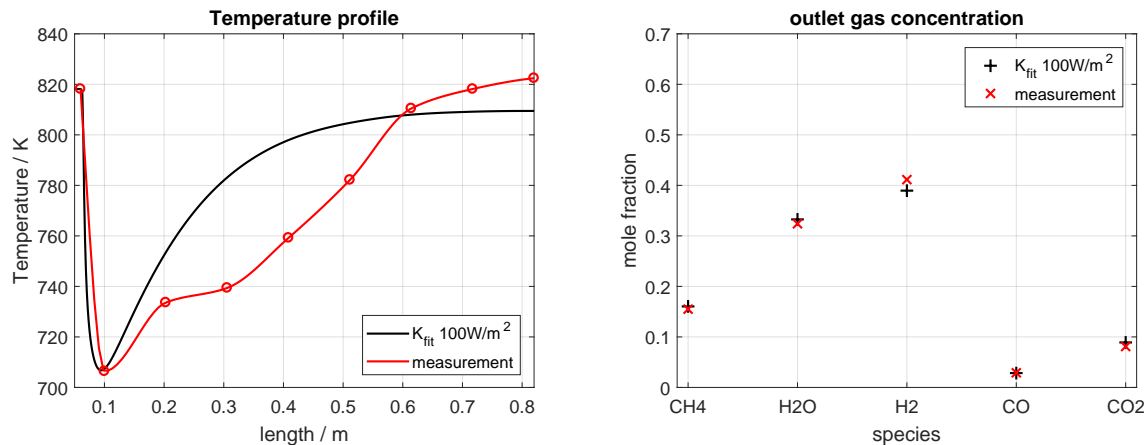
Since the discrepancy between  $K_{\text{Hoang}}$  and  $K_{\text{calc}}$  is most significant for  $\text{CH}_4 + \text{H}_2\text{O} \rightleftharpoons \text{CO} + 3\text{H}_2$ , only this equilibrium constant has been fitted and implemented in the AUCI model. The red line in Figure 4.22 shows the fitted values of the calculated equilibrium constant with the model function:

$$K_{\text{fit}} = 320701.4 \exp\left(17.6 - \frac{27060.7}{T}\right) \quad (4.1)$$

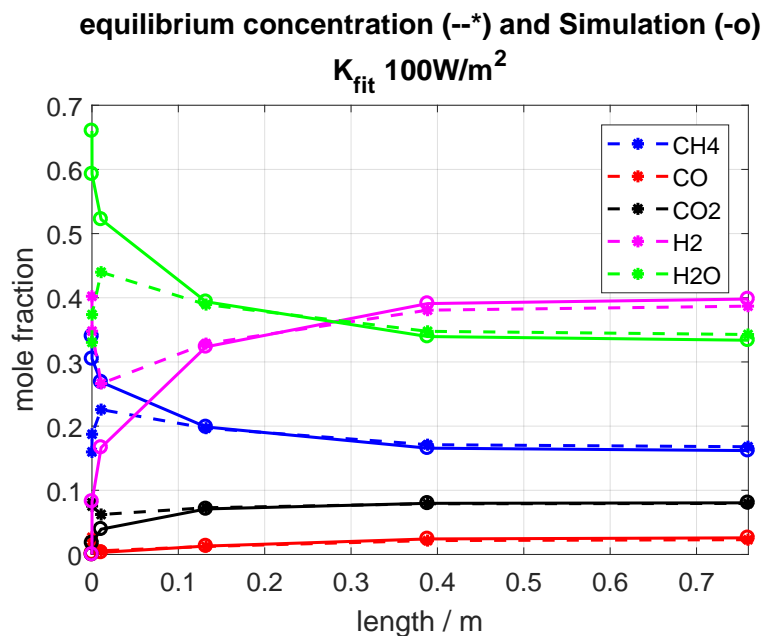


**Figure 4.22:** Comparison of different equilibrium constants. It shows the temperature dependency of Hoangs  $K_e$ , the calculated  $K_e$  and the model function for the calculated equilibrium constant.

The implementation of the model function in the AUCI model leads to the results depicted in Figure 4.23 where the outlet gas concentration differs only slightly from the measurement. The comparison with the Gibbs reactor is shown in Figure 4.24. It is depicted that, in the contrary to the simulations described in the previous sections, the simulation reaches equilibrium within the first 15 cm and stays in this equilibrium condition.



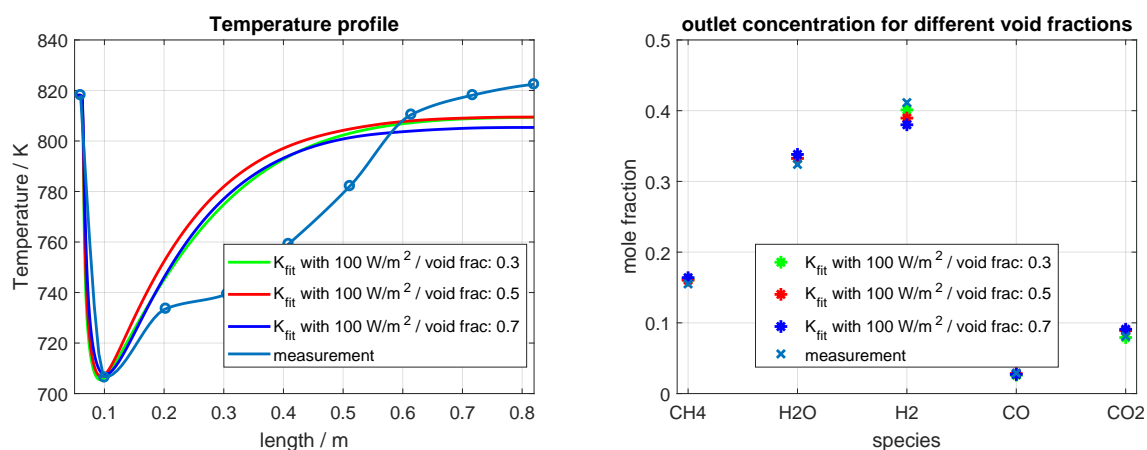
**Figure 4.23:** Comparison of simulated and measured values for Hoangs's kinetics with the equilibrium constant  $K_{fit}$  and  $100 \text{ W/m}^2$ . The left figure compares the polyline results for the flow temperature with the measurement. The right figure shows the deviation of the simulated mean outlet concentration from the measurement.



**Figure 4.24:** Comparison of simulation with the equilibrium constant  $K_{fit}$  and equilibrium concentration. The equilibrium concentration was calculated with the Gibbs reactor in MATLAB

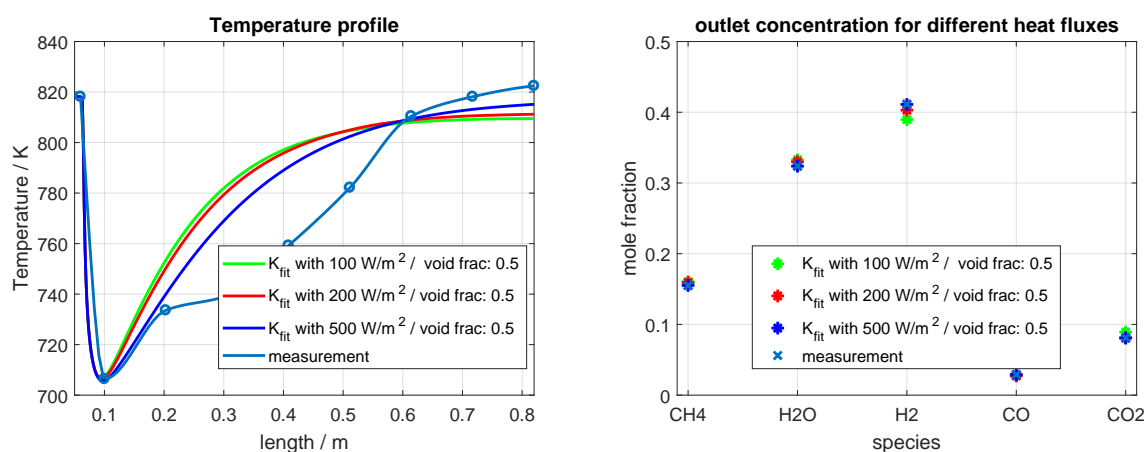
### 4.2.5 Parameter study with $K_{\text{fit}}$

For the understanding how unknown parameters influence the outcome, void fraction and heat flux are changed. Increasing the void fraction results in a smaller ratio of catalytic material in the reformer (see equation 2.71), which leads to a worse heat conduction. This is seen on the left side in Figure 4.25.



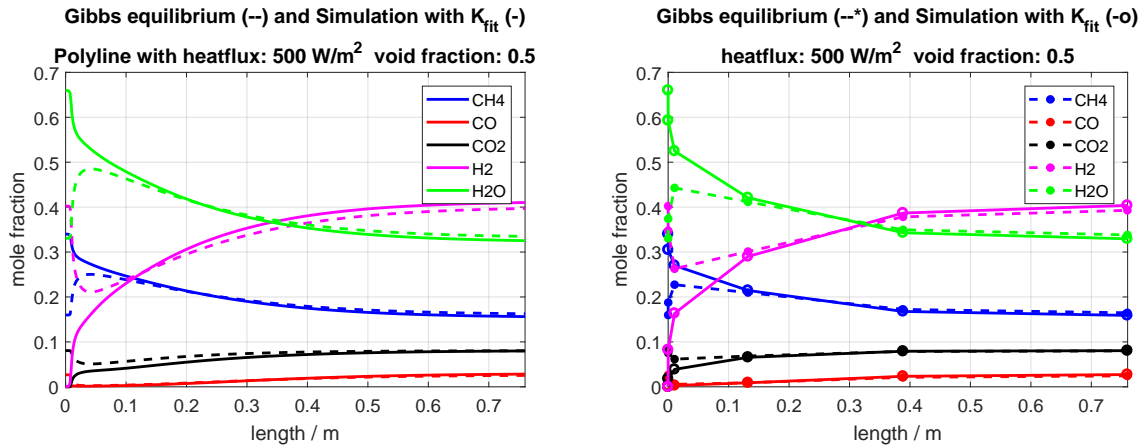
**Figure 4.25:** Comparison of simulated and measured values for Hoangs's kinetics with the equilibrium constant  $K_{\text{fit}}$ ,  $100 \text{ W/m}^2$  and different void fractions. The left figure compares the polyline results for the flow temperature with the measurement. The right figure shows the deviation of the simulated mean outlet concentration from the measurement.

The simulated outlet gas temperature differs from the expected value by approximately 15 K. To decrease this difference in temperature, the external applied heatflux was increased. The variation of the heat flux yielded the results in Figure 4.26.



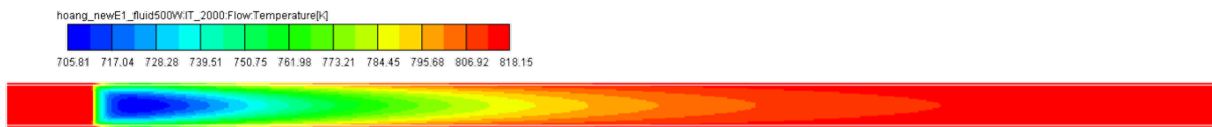
**Figure 4.26:** Comparison of simulated and measured values for Hoangs's kinetics with the equilibrium constant  $K_{\text{fit}}$ , void fraction of 0.5 and different heat fluxes. The left figure compares the polyline results for the flow temperature with the measurement. The right figure shows the deviation of the simulated mean outlet concentration from the measurement.

Figure 4.27 compares the polyline result with the mean values of the cuts.



**Figure 4.27:** Comparison of the deviation from Gibbs equilibrium for polyline result and mean values of cuts with a heatflux of  $500 \text{ W/m}^2$  and void fraction of 0.5. The equilibrium concentration was calculated with the Gibbs reactor in MATLAB

A typical temperature profile for the AVL reformer can be seen in Figure 4.28. Figure 4.29 shows the corresponding  $\text{H}_2$  generation. Both were calculated with a heat flux of  $500 \text{ W/m}^2$  and void fraction of 0.5. The gas temperature shows the expected behaviour, which is a fast decrease at the beginning of the catalyst due to the chemical reactions. The heat up with the applied heat flux is also shown in this figure. Due to the thermal conductivity, the outer regions of the model are heating up faster. The  $\text{H}_2$  mole fractions correlate to the temperature. The figures mentioned above show that the higher the temperature, the higher the  $\text{H}_2$  concentration which leads to a higher concentration at the outer regions of the reformer.



**Figure 4.28:** Flow temperature for the solid and fluid case at  $500 \text{ W/m}^2$  with  $K_{fit}$



**Figure 4.29:**  $\text{H}_2$  generation at  $500 \text{ W/m}^2$  with  $K_{fit}$

For a better comparison, a simulation of the benchmark model was redone with the calculated equilibrium constant. There is no significant discrepancy between the species

concentration calculated with the fitted equilibrium constant and the constant from the benchmark model (see Figure 4.30) but the mean temperature profile differs at its minimum by 50 K. Those temperature profiles are compared with literature [8] in Figure 4.31.

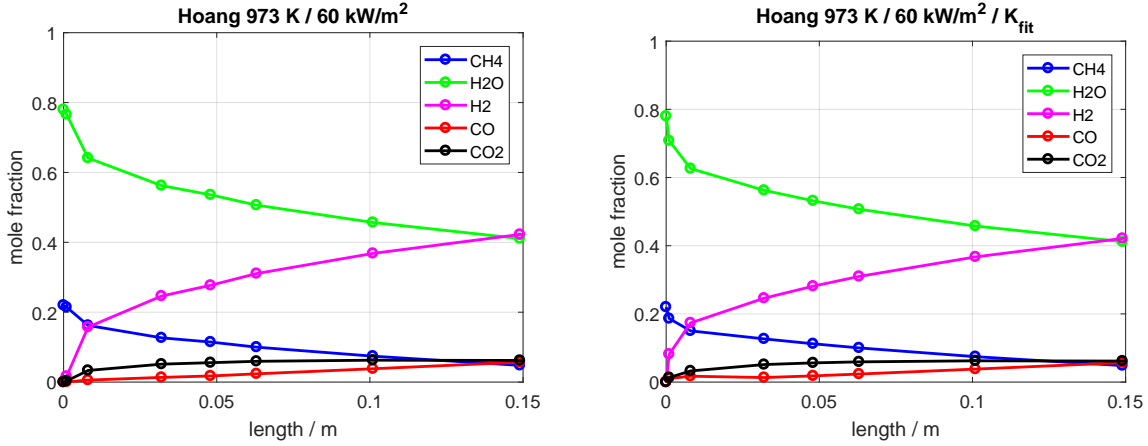


**Figure 4.30:** Comparison of mean mole fraction with different equilibrium constants for the benchmark model. The results of the left figure were calculated with Hoang’s equilibrium constant (the first in equation 3.8) and the results of the right figure were calculated with equation 4.1.

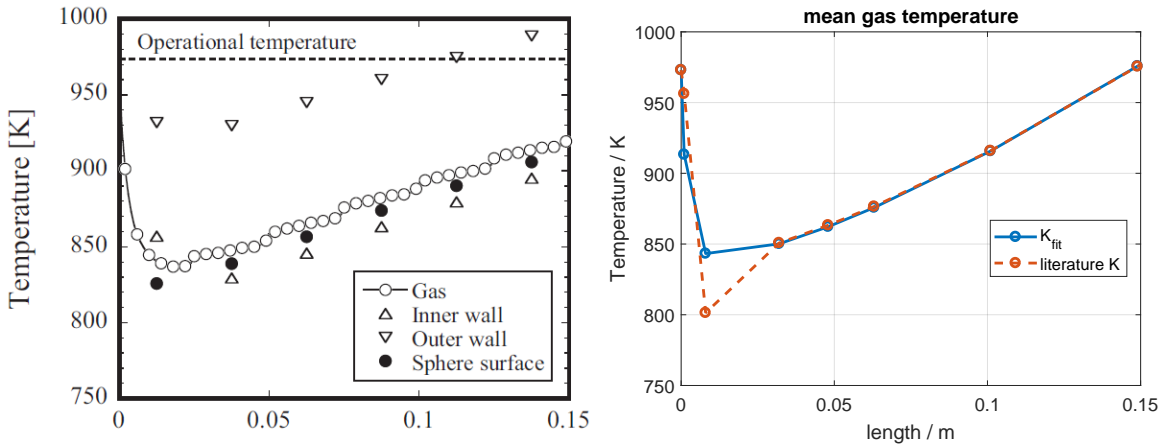


**Figure 4.31:** Comparison of simulated mean temperatures for the benchmark model (right) with the figure taken from Kuroki (left) [8]. The unit of both x-axis is in meter.  $K_{fit}$  indicates the gas flow temperature of the simulation with the fitted equilibrium constant, "literature K" indicates the gas flow temperature of the simulation with respect to the first equilibrium constant given in equation 3.8.

Additionally simulations were done with  $K_{fit}$  in combination with the kinetic parameters of Xu, which are shown in Table 4.2. The results of those simulations are compared to the simulations with  $K_{fit}$  and the kinetic parameters of Hoang (see Table 3.5) in the following figures. Figure 4.32 displays the simulations with a heat flux of  $100 \text{ W/m}^2$  and Figure 4.33 shows the simulations with a heat flux of  $500 \text{ W/m}^2$ . The difference in reaching the equilibrium concentration for the two kinetic sets is depicted in Figure 4.34.

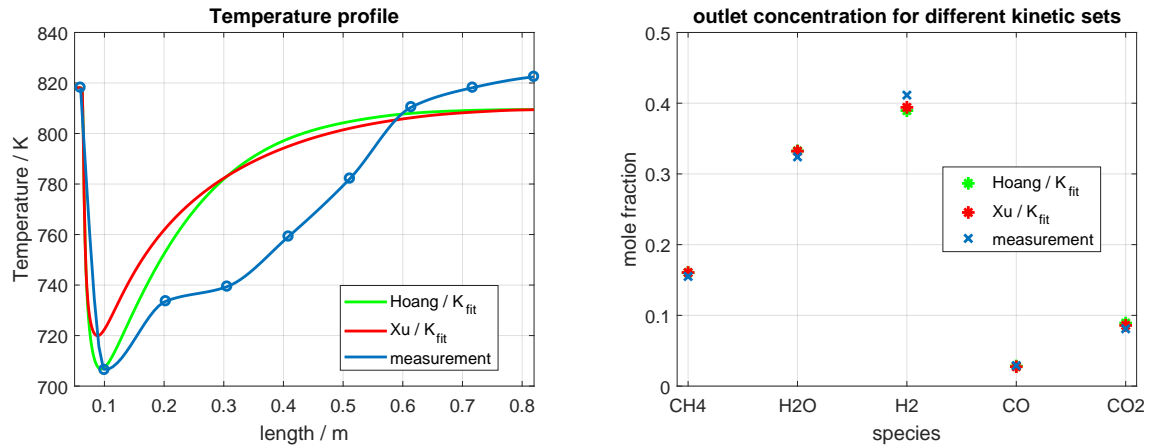


**Figure 4.32:** Comparison of simulated and measured values for Hoang's and Xu's kinetics with a heat flux of  $100 \text{ W/m}^2$  and void fractions of 0.5. The left figure compares the polyline results for the flow temperature with the measurement. The right figure shows the deviation of the simulated mean outlet concentration from the measurement.

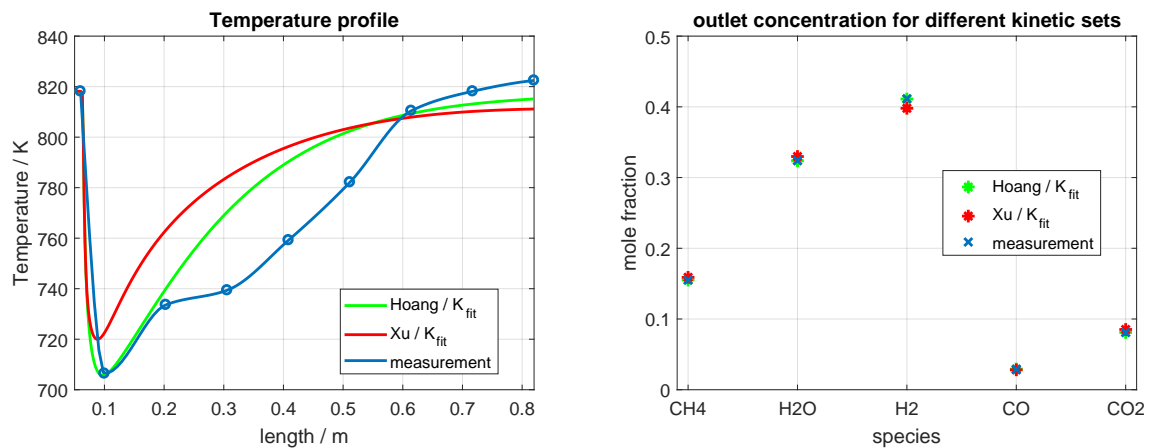


**Figure 4.33:** Comparison of simulated and measured values for Hoang's and Xu's kinetics with a heat flux of  $500 \text{ W/m}^2$  and void fractions of 0.5. The left figure compares the polyline results for the flow temperature with the measurement. The right figure shows the deviation of the simulated mean outlet concentration from the measurement.

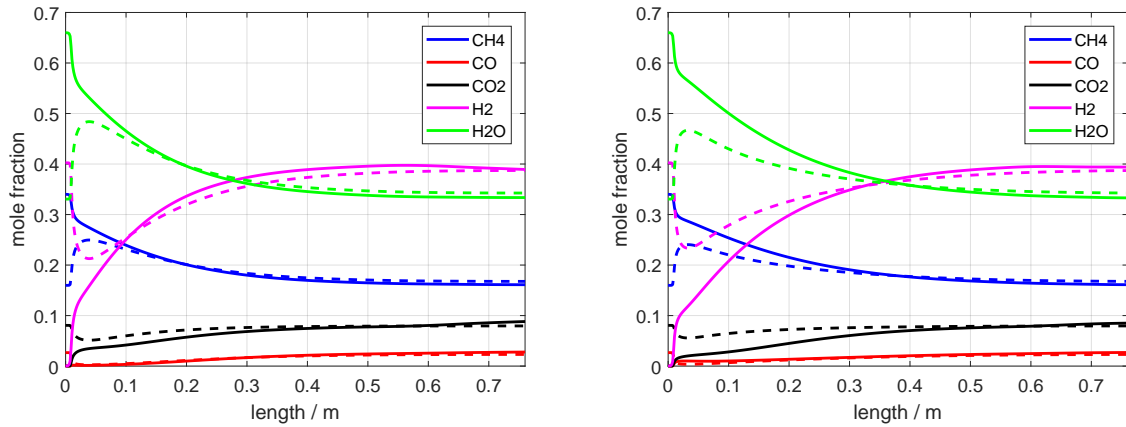


**Figure 4.34:** Mole fraction comparison of polyline results with the results of the Gibbs reactor with a heat flux of  $100 \text{ W/m}^2$ , void fraction of 0.5 and the model function for the equilibrium constant. The left figure shows the reformation process for the kinetic parameters of Hoang and the right figure for the kinetic parameters of Xu.

Figure 4.34 presents that the simulation with the parameters of Xu needs more reformer length for reaching the equilibrium concentration, although the pre-exponential factors have higher values. This leads to the conclusion that the activation energies have more influence in reaching the equilibrium than the pre-exponential factors, since the activation energies of Hoang have smaller values than the ones of Xu.

The optimum settings for the smallest deviation from the measurement can be taken from Table 4.4.

**Table 4.4:** Settings for the smallest deviation from the measurement

Pre-exponential factors	Hoang (Table 3.5)
Activation energies	Hoang (Table 3.5)
Adsorption constants	Hoang (Table 3.6)
Equilibrium constants	$K_{e1} = K_{fit}$ (equation 4.1) $K_{e2}$ from Hoang (equation 3.8) $K_{e3}$ from Hoang (equation 3.8)
Heat flux	$500 \text{ W/m}^2$
OFA	0.5

### Summary and Outlook

---

Model verification in AVL BOOST's 1-D environment was not leading to useful results because it does not allow the application of an external heat flux into the reformer unit. To simulate the influence of the heat flux, the specific heat of the reformer was modified to a non-physical value of 3000 kJ/(kg K) (see Figure 4.3 and 4.4). Only the 3-D model in FIRE, where an external heat flux was applied, showed a satisfying agreement to the literature results, which are shown in Figure 4.6. The failure to reach the equilibrium concentration in Figure 4.7 can be explained by the short reformer length of 15 cm. It seems like the concentration will reach its equilibrium, if the reformer length is increased or if higher inlet temperatures with a corresponding heat flux are used. This is implied by the diagram on the right side of Figure 4.7.

Kuroki [8] states that a heat flux of 60 kW/m<sup>2</sup> for an inlet gas temperature of 973 K and a heat flux of 85 kW/m<sup>2</sup> for an inlet gas temperature of 1073 K is needed to reach the inlet temperatures at the outlet. Figure 4.7 shows that the developed model is only in agreement for the lower temperature and heat flux with the values of Kuroki. This could be due to the use of different turbulence models or a different polynomial function for the calculations of material properties.

Applying the kinetic model of Hoang to the AVL reformer model led to strong deviations from expected values (see Figure 4.8). The first approach for overcoming this problem was to use different kinetic parameters from literature (see Table 4.2) which did not improve the results significantly (see Figure 4.11). Due to the fact that every catalyst has its own specific pre-exponential factors and activation energies for specific reactions, the use

of an optimization tool for reaching the expected values is justified, if measured data is available.

The optimization was done in AVL BOOST's 1-D environment, where it was not possible to consider an external heat flux during the optimization process. This led to an agreement of the outlet gas concentration and the expected concentration but the temperature profile deviates strongly from the measurement (see Figure 4.14).

Since the outlet concentration of all the previous described simulations (except the optimization) showed a deviation from equilibrium, the equilibrium constants of each partial reaction were investigated. This analysis showed that Hoangs equilibrium constant for the first partial reaction is only valid in his special case and for high temperatures where nearly all  $\text{CH}_4$  is reformed. His values differ by seven orders of magnitude to the calculated one in section 2.8.

The results of the simulations with the recalculated equilibrium constant showed a significant improve in reaching the expected values.

One way to validate this kinetic model with the model function for the equilibrium constant was to resimulate the literature benchmark. No significant difference was detected in the outlet concentration but the temperature profile was in better accordance with the values given by Kuroki [8] (Figure 4.31 and Figure 4.30).

Additional simulations were performed with the model function for the equilibrium constant with the kinetic parameters of Xu. The goal was to investigate, if the equilibrium concentration at the outlet can be reached with different kinetic parameters and the influence they have on the gas temperature and the speed of reaching the equilibrium. The analysis confirmed the assumption, that the kinetic parameters have only an influence on the speed of reaching the equilibrium and how much energy is needed for the reformation and not if the equilibrium can be reached at all (Figure 4.34).

Different void fractions lead to slightly different temperature profiles. It can be explained by a worse heat conduction and increasing flow velocity with increasing void fraction.

The 3-D results shown in Figure 4.28 and Figure 4.29 are given respectively for all 3-D results. The gas temperature shows the expected behaviour, which is a fast decrease at the beginning of the catalyst due to the chemical reactions. The heat up with the applied heat flux is also presented in this figure. Due to the thermal conductivity, the

---

outer regions of the model are heating up faster. The H<sub>2</sub> mole fractions correlate to temperature. The figures mentioned above show that the higher the temperature, the higher the H<sub>2</sub> concentration, which leads to a higher concentration at the outer regions of the reformer.

The optimum settings for the smallest deviation from the measurement are

Pre-exponential factors	Hoang (Table 3.5)
Activation energies	Hoang (Table 3.5)
Adsorption constants	Hoang (Table 3.6)
Equilibrium constants	K <sub>e1</sub> = K <sub>fit</sub> (equation 4.1) K <sub>e2</sub> from Hoang (equation 3.8) K <sub>e3</sub> from Hoang (equation 3.8)
Heat flux	500 W/m <sup>2</sup>
OFA	0.5

and are also shown in Table 4.4.

The results indicated, that this model could be used to simulate complex reformer geometries for example with shell and tube heat exchanger, which are often used in fuel cell applications. It has to be considered, that the equilibrium function was calculated for standard pressure and has to be recalculated for simulations with other pressure specifications. The deviation of the initial conditions for pressure from standard pressure were evaluated and due to its small influence neglected.

Further work could address the uncertainty quantification of the model. So far the results of simulations are taken, if specific convergence criteria have been reached. Ill-conditioned criteria can lead to converging solutions with physically wrong results. Therefore the minimum iteration length and the convergence criteria were altered, until their dependency on the outcome vanished. A problem is that no error can be derived from that. Furthermore, there is the possibility to validate the model under different constraints with additional experiments.



---

## Bibliography

---

- [1] James P Van Hook. Methane-steam reforming. *Catalysis Reviews—Science and Engineering*, 21(1):1–51, 1980. DOI: 10.1080/03602458008068059.
- [2] WW Akers and DP Camp. Kinetics of the methane-steam reaction. *AIChE Journal*, 1(4):471–475, 1955. DOI: 10.1002/aic.690010415.
- [3] JRH Ross and MCF Steel. Mechanism of the steam reforming of methane over a coprecipitated nickel-alumina catalyst. *Journal of the Chemical Society, Faraday Transactions 1: Physical Chemistry in Condensed Phases*, 69:10–21, 1973. DOI: 10.1039/F19736900010.
- [4] SSEH Elnashaie, AS Al-Ubaid, MA Soliman, and AM Adris. On the kinetics and reactor modelling of the steam reforming of methane—a review. *Journal of Eng. Sci.*, 14(2):247–273, 1988.
- [5] Jianguo Xu and Gilbert F Froment. Methane steam reforming, methanation and water-gas shift: I. intrinsic kinetics. *AIChE journal*, 35(1):88–96, 1989. DOI: 10.1002/aic.690350109.
- [6] DL Hoang, SH Chan, and OL Ding. Kinetic and modelling study of methane steam reforming over sulfide nickel catalyst on a gamma alumina support. *Chemical Engineering Journal*, 112(1-3):1–11, 2005. DOI: 10.1016/j.cej.2005.06.004.
- [7] Anubhav Pratap Singh, Siddhartha Singh, Somenath Ganguly, and Anand V Patwardhan. Steam reforming of methane and methanol in simulated macro & micro-scale membrane reactors: Selective separation of hydrogen for optimum conversion. *Journal of Natural Gas Science and Engineering*, 18:286–295, 2014. DOI: 10.1016/j.jngse.2014.03.008.

- [8] Mayu Kuroki, Shinichi Ookawara, and Kohei Ogawa. A high-fidelity CFD model of methane steam reforming in a packed bed reactor. *Journal of Chemical Engineering of Japan*, 42(Supplement.):s73–s78, 2009. DOI: 10.1252/jcej.08we256.
- [9] Inc EG & G Technical Services. *Fuel Cell Handbook*, volume 7. U.S. Department of Energy, Office of Fossil Energy, 2004.
- [10] Samira Bagheri. *Catalysis in Fuel Cells (PEMC, SOFC)*. Springer International Publishing, Cham, 2017. DOI: 10.1007/978-3-319-43104-8\_3.
- [11] AVL List GmbH. CFD Solver, 2017.
- [12] Martin Berggren Dan S. Henningson. Fluid dynamics, theory and computation, 2005.
- [13] Joel H Ferziger and Milovan Peric. *Computational Methods for Fluid Dynamics*. Springer-Verlag Berlin Heidelberg, 2002. DOI: 10.1007/978-3-642-56026-2.
- [14] Charles Hirsch. *Numerical computation of internal and external flows: The fundamentals of computational fluid dynamics*. Elsevier, 2007.
- [15] Joseph Pedlosky. Notes for the MIT/WHOI Joint Program Course 12.800, Fluid Dynamics of the Atmosphere and Ocean "Chapter 3: The Stress Tensor for a Fluid and the Navier Stokes Equations". <http://www.whoi.edu/sbl/liteSite.do?litesiteid=107533&articleId=197629>, 2014.
- [16] Rosenqvist Kochukhov, Pavlenko. Fluid mechanics compendium. Department of Physics and Astronomy Uppsala University, 2017.
- [17] AVL List GmbH. Species Transport, 2017.
- [18] AVL List GmbH. Aftertreatment, 2017.
- [19] Michael E Coltrin, Robert J Kee, Fran M Rupley, and Ellen Meeks. Surface chemkin-iii: A fortran package for analyzing heterogeneous chemical kinetics at a solid-surface-gas-phase interface. Technical report, Sandia National Labs., Albuquerque, NM (United States), 1996.
- [20] Hans Dieter Baehr and Karl Stephan. *Wärme-und Stoffübertragung*, volume 2. Springer, 1996. DOI: 10.1007/978-3-662-10837-6.
- [21] Manfred Klell. Höhere Thermodynamik, 2012.

- 
- [22] [https://de.wikibooks.org/wiki/Tabellensammlung\\_Chemie/\\_spezifische\\_WaermeKapazitaeten](https://de.wikibooks.org/wiki/Tabellensammlung_Chemie/_spezifische_WaermeKapazitaeten), visited on the 10<sup>th</sup> of September, 2018.
- [23] Barin Ihsan. *Thermochemical data of pure substances*, volume 2. Weinheim, 1993.
- [24] Barin Ihsan. *Thermochemical data of pure substances*, volume 3. Weinheim, 1995.
- [25] Michael Müller. Thermodynamische Daten bei 25C. <http://www.chempage.de/Tab/thermo.htm>.
- [26] Giuseppe Somare. Diesel Reforming Medium and Long Run Tests. Master's thesis, Technische Universität Wien, Austria, unknown.
- [27] Karin Fasching. Untersuchungen zu Diesel-Steam-Reforming für SOFC-Systeme. Master's thesis, Technische Universität Wien, Austria, 2015.
- [28] SSEH Elnashaie, AM Adris, AS Al-Ubaid, and MA Soliman. On the non-monotonic behaviour of methane—steam reforming kinetics. *Chemical Engineering Science*, 45(2):491–501, 1990. DOI: 10.1016/0009-2509(90)87036-R.
- [29] Verein Deutscher Ingenieure. VDI-Waermeatlas, Berechnungsblaetter fuer den Waermeuebergang., 1994.
- [30] Klaus Schittkowski. NLPQL: A FORTRAN subroutine solving constrained nonlinear programming problems. *Annals of operations research*, 5(2):485–500, 1986. DOI: 10.1007/BF02022087.
- [31] Robert Leinfelder. Reaktionskinetische Untersuchungen zur Methan-Dampf-Reformierung und Shift-Reaktion an Anodenoxidkeramischer Brennstoffzellen.



---

# Acknowledgement

---

First of all, I would like to thank my supervisor at AVL, DI Michael Seidl, for the opportunity to work on such an interesting topic. The discussions with him were essential for the promising results of this thesis.

I would also like to thank my supervisor at the TU Graz, Univ.-Prof. Dipl.-Phys. Dr.rer.nat. Wolfgang von der Linden, who made this cooperation between AVL and TU Graz possible, and for pushing me in the right direction to get a better understanding about the theoretical background of CFD simulations.

I have to express my gratitude to Dr. Thomas Mitterfellner and Dr. Thirumalesha Chittipotula from AST department, for their help regarding the implementation of the kinetic models in BOOST and FIRE.

I also have to thank the team of Dr. Robert Pöschl at DAC, for helping me with problems related to FIRE.

Last but not least, I would like to thank my family and my friends for their support and help throughout the years. It would not have been possible without you!